Development and Validation of a Tailsitter UAV for Efficient Hover and Forward Flight

by

Vinamr Arya

A Thesis Presented in Partial Fulfillment
of the Requirements for the Degree
Master of Science

Approved April 2025 by the
Graduate Supervisory Committee:

Anthony Waas, Chair
Spring Berman
Anthony Wende

ARIZONA STATE UNIVERSITY

May 2025

ABSTRACT

This thesis presents the design, development, and testing of a tandem-wing tail sitter eVTOL aircraft capable of seamless vertical takeoff and landing (VTOL) and efficient forward flight without the mechanical complexity of tilt-rotor systems or added weight of hybrid propulsion systems. The work began with preliminary sizing and aerodynamic analyses in VSPAero to determine optimal wing incidence and aspect ratio for stable cruise performance. A refined configuration was then reanalyzed using a higher fidelity model to examine interaction effects between the front and rear lifting surfaces. Structural design centered on a 3D-printed fuselage and modular wing components, employing selective reinforcement and minimal infill strategies to achieve high strength to weight ratio. Ground tests included tethered hover trials and free-flight evaluations under manual pilot control, confirming stable roll, pitch, and yaw authority. Despite incorporating fewer moving parts than traditional tiltrotors, the aircraft demonstrated reliable vertical takeoff, controlled transitions, and steady forward flight at speeds consistent with the tandem-wing's lift requirements. Preliminary measurements showed the design could achieve approximately eight minutes of flight while carrying a 0.5 kg payload across an effective range of about 8 km. Collectively, these results indicate that a tandem-wing tail sitter can offer a simpler, more efficient VTOL solution, laying groundwork for future refinements and potential scaling to larger or more autonomous platforms.

DEDICATION

To my parents—those who gave me life, those who nurtured me through it, and those who embraced me as their own. Your unwavering support, patience, and boundless love have been the foundation upon which all my dreams have been built. Your sacrifices, belief in me, and encouragement have guided every step I've taken. This achievement belongs as much to you as it does to me. Thank you for always being there for me.

ACKNOWLEDGMENTS

Research rarely follows a straight path, and this project certainly did not. The people and places listed here turned every detour into an opportunity and every obstacle into a lesson I will carry forward.

First and foremost, I express my deepest gratitude to my advisor, Dr. Anthony Waas for his unwavering support, steady confidence in my abilities, and the financial backing that made this research a reality. His mentorship fostered both the technical depth of this project and my own professional growth. I am also grateful to my committee members, Dr Spring Berman and Professor Wende whose thoughtful insights and constructive feedback consistently sharpened the scope and rigor of this thesis.

Within our research group, I sincerely thank several colleagues who offered indispensable assistance. Dr. Minhazur Rahman guided the Abaqus impact-survivability simulations and provided invaluable guidance well beyond his formal duties. Vitesh Patel supplied hands-on help throughout the structural and outdoor testing campaigns, ensuring reliable data and safe laboratory practice.

I would also like to acknowledge Blue Flite for introducing rapid aircraft design and fabrication workflows. Their approach to iterative prototyping significantly accelerated the development cycle of this tandem-wing tailsitter.

Finally, I thank the School for Engineering of Matter, Transport and Energy (SEMTE) and Arizona State University for the facilities, funding mechanisms, and collaborative atmosphere that sustained every stage of this work.

TABLE OF CONTENTS

Page

LIST OF TABLES

Table Page

LIST OF FIGURES

Figure Page

CHAPTER 1

INTRODUCTION

This thesis investigates the conceptualization, design, and testing of a tandem-wing tail sitter eVTOL aircraft featuring a gull and inverted-gull wing configuration. The need for simpler, more efficient and versatile Unmanned Aerial Vehicles (UAVs) for rapid deployment—particularly in medical supply delivery and other time-critical missions—motivates this research. By leveraging a tailsitter concept, this design aims to combine vertical takeoff and landing (VTOL) convenience with the efficiency of conventional forward flight, all while minimizing the complexity of traditional hybrid propulsion systems or tilt-rotor mechanisms.

1.1 Background and Motivation

Electric vertical take-off and landing (eVTOL) aircraft have emerged as a dynamic area of innovation in aerospace, with over 130 new concepts proposed in the past decade. These designs, enabled by advances in battery technology and electric propulsion, promise quieter and more efficient short-range flight compared to conventional helicopters or fixed-wing aircraft needing runways.

Within the eVTOL domain, tailsitter concepts stand out for blending the key advantages of a quadrotor (vertical lift, maneuverability) with the efficiency of a fixed-wing airplane. By rotating the entire airframe 90 degrees rather than tilting or adding separate lift mechanisms, tailsitters eliminate much of the weight and drag penalty associated with traditional tiltrotor or large multi-boom designs. This simple pivot

approach helps maintain a better-aligned center of gravity (CG) for both hover and forward flight.

Seeking to maximize payload capacity, pitch stability, and overall aerodynamic efficiency, the present design incorporates a tandem-wing layout with two motors mounted on each wing. Such a layout promises improved lift distribution and load sharing—important for UAVs where every kilogram saved can be redirected toward payload or battery capacity. Building upon this concept, gull and inverted-gull wing geometries were adopted to reinforce structural rigidity, reduce fuselage frontal drag, and ensure smoother airflow around the airframe in forward flight.

Another essential objective was to develop a modular, 3D-printed drone platform for straightforward manufacturability and maintenance. By minimizing mechanical complexity—opting not to include extra tilt mechanisms or a dedicated tail rotor—the design contains fewer potential points of failure, which in turn streamlines the certification process under emerging FAA guidelines for sUAS. A simpler control system (relying on thrust vectoring and well-placed lifting surfaces) ensures that redundancy is built in without resorting to additional moving parts.

Such a UAV is well-suited for rapid deployment missions, whether delivering medical supplies to remote locations or providing real-time aerial surveillance. Its agile hover mode and efficient forward flight offer versatility across various applications, while the modular construction and reduced complexity help meet practical needs for certification, cost-effectiveness, and safe, reliable operations.

1.2 Problem Statement

The core challenge addressed by this thesis is achieving efficient hover and cruise capabilities in a single airframe without resorting to elaborate tilt mechanisms, additional propulsion systems, or even control surfaces. The design must:

- Take off and land vertically in confined spaces,
- Transition smoothly from hover to forward flight (and vice versa) without destabilizing aerodynamic behaviors
- Maintain stable forward flight

The vehicle's tandem-wing, gull + inverted-gull geometry and lack of a vertical stabilizer introduce unique structural and control challenges. Balancing low structural weight with sufficient rigidity, ensuring aerodynamic efficiency, and maintaining robust flight control are therefore central tasks.

1.3 Objectives and Scope

The primary objective of this thesis is to design, build, and test a tandem-wing tail sitter eVTOL that leverages gull and inverted-gull wings to achieve vertical takeoff, transition flight, and stable forward-flight modes. This includes:

- Developing the Aerodynamic Layout: Determining appropriate wing incidences, aspect ratios, and gull angles to balance lift, drag, and stability across flight regimes.

- Implementing the Avionics and Control Architecture: Developing a thrust-vector-based control strategy for vertical and fixed wing flight, particularly to manage yaw and roll without a dedicated vertical stabilizer.
- Prototyping and Testing: Fabricating a scaled aircraft to validate the design in ground tests, hover trials, and forward-flight evaluations.

The scope focuses on aerodynamic design, structural considerations, propulsion sizing, and flight control and manufacturing. Broader topics like commercial certification or highly autonomous swarming algorithms lie outside the immediate scope but may be proposed as future work.

1.4 Thesis and Organization

Following this Introduction in Chapter 1, the thesis is structured as follows:

- Chapter 2: Literature Review surveys existing eVTOL concepts, tailsitter configurations, tandem-wing theory, and gull-wing applications, concluding with identified gaps and the proposed research contributions.
- Chapter 3: Conceptual Design lays out the mission requirements, initial configuration decisions, propulsion layout, and control considerations for the tandem gull-wing tailsitter.
- Chapter 4: Detailed Design and Analysis delves into aerodynamic, structural, propulsion, and flight-control analyses using tools like VSPAero.
- Chapter 5: Avionics and Controls Architecture covers test methodology, hover data, and preliminary results.

- Chapter 6: Testing discusses the flight test plan, transition performance, forward-flight handling, and compares findings with design predictions.
- Chapter 7: Airworthiness documents the plan and simulations for the UAV to meet the safety requirements laid out by the FAA for operations over populated areas.
- Chapter 8: Conclusion and Future Work summarizes key findings, contributions, limitations, and outlines potential avenues for advancing this research.

Finally, References and Appendices provide additional engineering drawings and data, MATLAB code, and additional results for completeness.

CHAPTER 2

LITERATURE REVIEW

2.1 Overview of eVTOL and Tailsitter Configurations

eVTOL concepts can be broadly categorized by how they produce lift in hover versus cruise. Wingless multicopters (e.g. Volocopter VoloCity, EHang 184) use multiple rotors and no wing, trading excellent hovering efficiency for poor range due to lack of lift in forward flight (Bacchini & Cestino, 2019). Lift + Cruise designs employ separate systems: dedicated vertical lift propellers and a separate propeller or jet for cruise thrust.

Figure 1: Wisk Cora VTOL aircraft

For example, the Wisk/Kitty Hawk Cora air-taxi has wing-mounted lift rotors for takeoff and a rear pusher propeller for cruise. This separation simplifies control and transition (each propulsion optimized for its flight mode) at the cost of carrying dead weight during portions of flight. Vectored thrust designs use the same propulsion devices for both hover and forward flight by tilting or redirecting thrust. This includes tilt-rotor aircraft like Joby Aviation's S4 (which tilts its propellers) and tilt-wing or tilt-duct concepts like the Lilium Jet (which embeds numerous electric ducted fans that pivot with the wing). Vectored designs benefit from having a wing for efficient cruise and avoiding redundant lift systems, but they involve complex mechanics or control to safely reorient thrust during transitions. A final category is electric helicopters (eHelos) – essentially conventional rotorcraft with electric drive – and hover bikes, but these are less common and more niche (Bacchini & Cestino, 2019). Tailsitters uniquely simplify propulsion by eliminating mechanical tilt mechanisms entirely, instead rotating the entire airframe to transition between vertical and horizontal flight modes. This yields a mechanically simpler architecture; however, it introduces considerable challenges in attitude control during transitions, necessitating sophisticated thrust-vectoring or aerodynamic control strategies. A comparative study found that pure multicopters excel at hovering efficiency, vectored-thrust "flying wing" jets excel at fast cruise and range, while lift + cruise hybrids strike a compromise in performance (Bacchini & Cestino, 2019). Table 1 summarizes key features of major eVTOL configurations, including tail sitters, for comparison.

Type	Aircraft	Approach	Pros	Cons
Multicopter	Ehang 184	Multiple propulsion systems	Simple design, low disk loading	Low forward speed, poor range
Lift + Cruise Propulsion	Wisk Cora	Separate lift and cruise prop/wing	Simplified control & transition (no moving parts); optimized lift and cruise devices	Carries extra weight; added system complexity (multiple propulsion sets).
Tilt-Rotor (Vectored)	Bell V-22 Osprey	Winged aircraft with rotors that tilt for vertical or forward thrust	Efficient hover comparable to helicopter; full wing for efficient cruise; avoids retreating blade issue in high-speed flight	Complex tilt mechanisms; potential single-point failure; transitioning rotors induce gyroscopic and control issues to manage
Tilt-Wing	Airbus Vahana	Entire wing (with propellers) rotates between hover and cruise orientations	Wing avoids airflow impingement during hover (better lift); wing *blown* by props at high AoA, augmenting lift	Low pitch control power in hover; mechanically complex; engine failure can cause severe imbalance
Tailsitter	NASA Puffin	Entire aircraft pitches up 90° to take off/land on its tail	mechanically simple (no tilt hinges)	Difficult attitude control during transition

Table 1 – Comparison of E-VTOL/Tailsitter Configurations and Their Key Features.

2.2 Tandem Wing Configurations

Tandem-wing aircraft have two main lifting wings, one forward and one aft, with the center of gravity between them. This layout is distinct from a conventional airplane (which has one main wing and a much smaller tail) and from canard designs (which have a small foreplane). In a tandem, both wings contribute significant lift in cruise.

Historically, tandem wings have been experimented with for over a century – examples range from the 1922 Peyret glider to the 1930s Mignet “Flying Flea” (Pou-du-Ciel) homebuilt. The tandem arrangement offers some potential aerodynamic advantages. By spreading lift between two widely separated wings, induced drag can be reduced; analyses and wind tunnel tests have shown tandem-wing designs can achieve a lower overall drag coefficient over a range of lift conditions. Essentially, each wing can operate at a lower lift loading, improving the spanwise lift distribution efficiency similar to a biplane without the interference of stacked wings (especially if the wings are staggered vertically to avoid the aft wing sitting fully in the front wing’s wake, which is the case for our aircraft).

Figure 2: Tandem Wing Aircraft

However, tandem wings come with notable stability and trim challenges. Longitudinal static stability requires that the aft wing reduce its lift as the angle of attack increases (so the aircraft naturally restores itself to level flight). This usually means the aft wing must be set at a lower lift coefficient or smaller size relative to the front, akin to how a tailplane carries negative lift in a conventional plane.

In practice, early tandem designs like the Flying Flea suffered disastrous stability problems: at certain angles, the front wing would stall while the rear wing was still lifting, pitching the nose up and preventing recovery – a flaw that caused fatal accidents. Designers learned that to ensure stall progression (front wing stalling first), the aft wing often needs to be less loaded and/or have different incidence. Achieving proper longitudinal stability also often forced the center of gravity far forward between the wings. An analysis by Kostić et al. noted that in order for a tandem-wing aircraft to be stable, the CG had to be significantly forward of the midpoint between the wings' aerodynamic centers, which in turn prevented the aircraft from operating at its optimal lift distribution and maximum lift-to-drag ratio (Andrews & Perez, 2017). In other words, there is an inherent conflict: a tandem wing can reach a high efficiency if the lift is shared optimally, but doing so may undermine stability margins.

Despite these issues, tandem-wing and related joined-wing or box-wing concepts continue to intrigue researchers. The tandem arrangement offers benefits like a wide allowable center-of-gravity range and strong pitch authority (since both wings can be used to trim). A tandem design can tolerate larger shifts in payload or fuel load without becoming untrimmed – a potential advantage for cargo UAVs or variable payload operations. Modern studies (e.g., Kostić et al. 2022 on dynamic stability of tandem

UAVs) use computational methods to analyze stability across configurations and propose control strategies to mitigate instability (Figat, 2022). Some solutions include giving the aft wing slightly less span or different airfoil, so it stalls later, or even using active control surfaces to adjust lift distribution in real time. There has also been exploration of closed tandem wings (joined at the tips to form a loop or box) which can alleviate some induced drag and stability problems by effectively creating a continuous planar wing – though these introduce structural complexity.

2.3 Gull Wing and Inverted Gull Wing Concepts

Gull wings—characterized by their distinctive bend at the wing root—historically emerged primarily due to practical and structural considerations rather than solely aerodynamic optimization. However, gull-wing designs significantly influence aerodynamic and stability behavior. Barbosa and Catalano (2004) investigated gull-wing designs experimentally, demonstrating that their geometry considerably affects lateral stability, primarily via dihedral effects. A normal gull wing has an upward bend at the wing root (anhedral on the inner wing, dihedral outboard), whereas an inverted gull wing angles downward near the fuselage then back up toward the tips. A normal gull wing has an upward bend at the wing root (anhedral on the inner wing, dihedral outboard), whereas an inverted gull wing angles downward near the fuselage then back up toward the tips. Gull wings have appeared in aircraft design primarily for structural and practical reasons, though they also have aerodynamic effects.

Figure 3: Inverted Gullwing on the F4U Corsair

Aerodynamically, aside from stall and drag considerations, gull wings have some effect on lateral stability. An upwards-angled inner wing (normal gull) provides dihedral effect (increasing roll stability), while an inverted gull provides an anhedral effect (improving roll rate and accommodating other stability needs if the aircraft is high-wing). In practice, designers choose gull vs inverted gull based more on practical geometry than pure aerodynamics. For example, an inverted gull on a low-wing fighter solved landing gear issues; a normal gull on a high-wing glider solved cockpit visibility and ground clearance issues. Both types fell out of favor post-1950s as jet engines and tricycle landing gear removed many of the original constraints.

2.4 Knowledge Gaps

This review highlights that while there is rich literature and many prototypes for each concept – eVTOL configurations, tailsitters, tandem wings, and gull wings – there are also gaps where further research is needed, especially in the intersections of these areas. For

eVTOL aircraft, one gap is in high-fidelity understanding of transition flight dynamics. Many designs are flying, but the public literature on how to optimally control the transition (especially in turbulent urban environments or with partial failures) is still developing. Continued research on robust control strategies for hybrid VTOL (tiltrotors, tailsitters, etc.) is critical to make these vehicles safe. Another gap is system optimization as shown by Bacchini & Cestino (2019), the "best" eVTOL design depends on the mission. There is no consensus yet on how to quantitatively choose one configuration over another for a given urban air mobility use case – more studies introducing standardized metrics or efficiency indices will help guide designers. Furthermore, tailsitter-specific challenges in transition-flight dynamics remain inadequately explored, especially for configurations featuring complex aerodynamic interactions between tandem and gull-wing elements. Similarly, although Andrews and Perez (2017) and Zhang et al. (2023) provide valuable theoretical insights into tandem-wing aerodynamics and stability, practical implementation and experimental validation for tandem wing and gull wing geometry—particularly in small-scale UAV applications—remain limited.

Consequently, this thesis attempts to address some of these gaps by combining insights from tandem-wing aerodynamics, gull-wing stability effects, simplified tailsitter propulsion concepts, and modern additive manufacturing techniques to deliver a robust, versatile UAV.

CHAPTER 3

CONCEPTUAL DESIGN

3.1 Initial Configuration

Figure 4: Initial Prototype for the UAV

3.1.1 Early I-Beam Design

Initially, the aircraft was conceived as a tandem wing layout with two identical straight wings featuring elliptical wingtips, connected by two diagonal members along the center. At the intersection of these diagonal members lay the fuselage. When viewed head-on in forward-flight orientation, this structure resembled an I-beam:

- “Flanges”: The front and rear wings.
- “Web”: The two central diagonal members forming the primary beam.

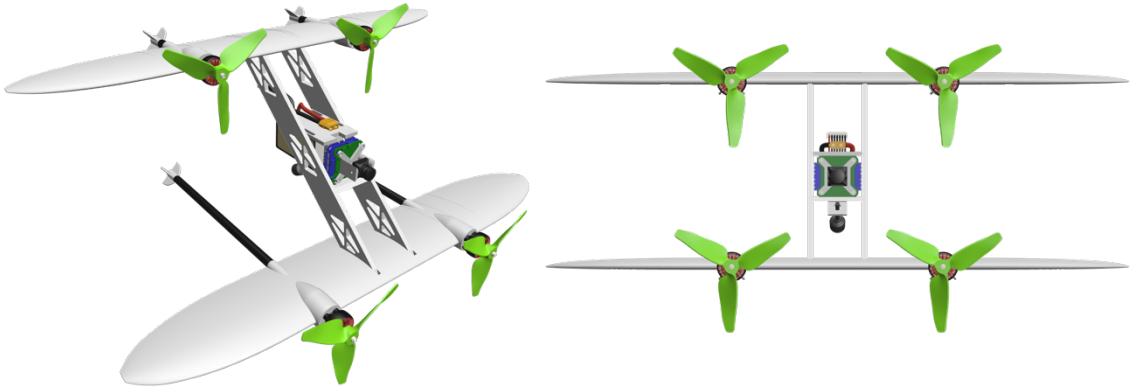

Figure 5 - Front left Isometric View (left), Front View (right) of first Iteration

Each wing had two motors (one on each side of the fuselage), resulting in a four-motor (quad) configuration in hover. The same motors provided forward thrust, with differential thrust vectoring for control. However, this arrangement introduced a torsional twist issue in the fuselage and diagonal cross members: when the motors produced yaw moments, the entire I-beam assembly twisted, indicating insufficient torsional rigidity. Instead of adding diagonal cross members to reinforce the existing design, as doing so would have contributed to drag.

3.1.2 Transition to an X-Frame Fuselage

To address the torsional flexibility, the design evolved to a conventional tubular fuselage flanked by an inverted gull wing in the front and a normal gull wing in the rear. Motors were placed at each wing “kink,” where the dihedral or anhedral angle changes, effectively clustering drag sources (motor nacelles, propellers, kink in wing geometry)

into one region. From the front view, the new layout forms an X-shaped frame, a more typical structure for quadrotors that reduces unwanted twisting.

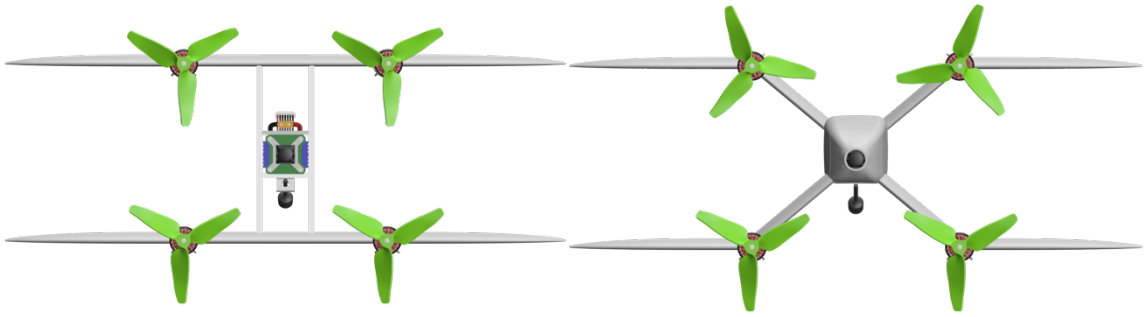

Figure 6 - Front View I - Frame (left), Front View X - Frame (right)

By simplifying the hover mechanism—relying on the same four motors for both vertical lift and forward propulsion—the design avoids the complexity of tilt-rotors or dedicated lift fans while ensuring the center of gravity in each flight mode is optimally placed. The trade-off is that thrust vectoring must be robust enough to provide yaw and roll authority during hover and to maintain stable forward flight without aerodynamic control surfaces.

3.2 Propulsion Layout and Wing Geometry

Gull wings have appeared in aircraft design primarily for structural and practical reasons, though they also have aerodynamic effects. This layout ensures the motors are placed at the same location as the previous design, maintaining equidistant moment arms from the CG in vertical orientation.

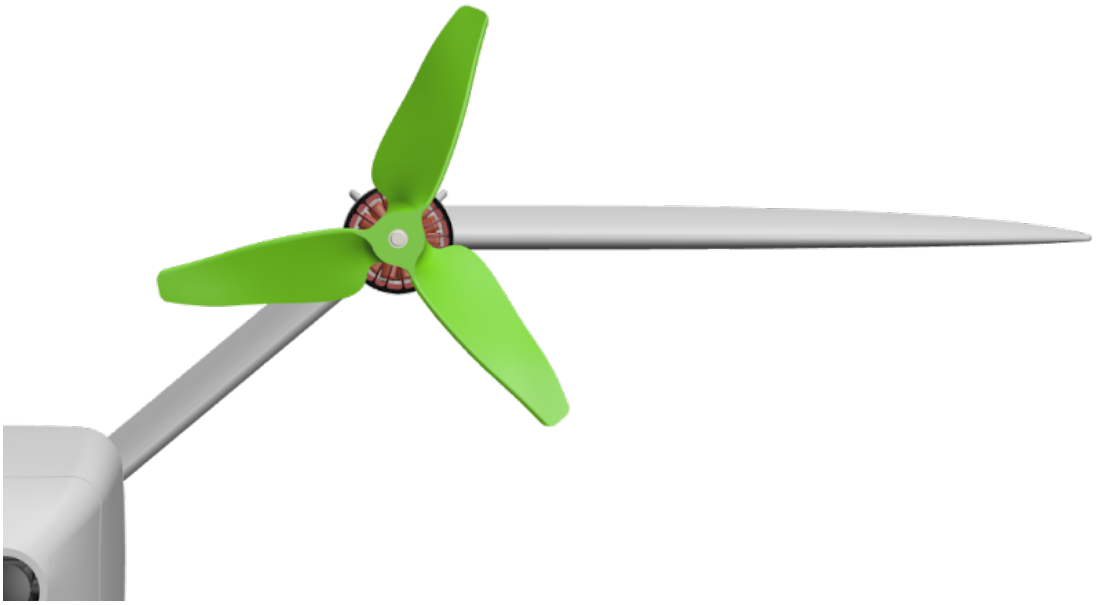

Figure 7: Rear Gull Wing (front view)

Aerodynamically, this shape provides multiple benefits:

- Lift and Stability:

  The forward inverted gull acts somewhat like an inverted V-tail, generating lift and contributing to pitch and roll stability once in forward flight. The rear gull portion functions similarly to a conventional V-tail, offering additional directional and roll stability, aided by the dihedral effect.

- Drag Reduction:

  Placing the motors at the gull "kinks" consolidates two potential drag sources (the angular junction and the motor nacelle) into one area subsequently minimizing interference drag by preventing multiple abrupt flow discontinuities along the wing.

3.3 Stability and Control Considerations

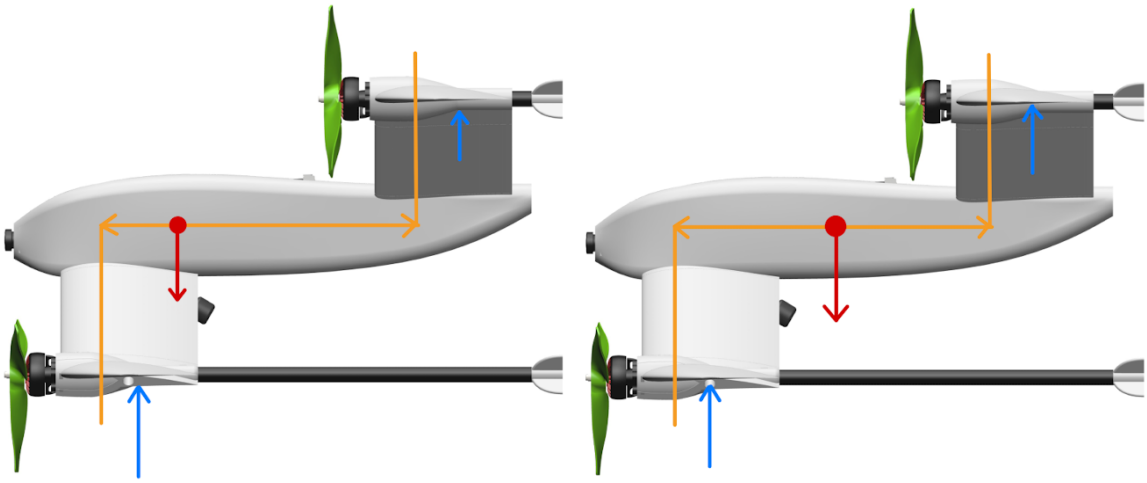

Figure 8: CG (red) Position for Stable Configuration (left), CG for Unstable Configuration (right)

The inherent pitch instability in a tandem-wing layout requires careful balancing of lift (blue in Figure 8) forces between the front and rear wings:

- The center of gravity (CG) (red in Figure 8) is placed forward of the aircraft's aerodynamic center to maintain a nose-heavy layout.
- To ensure stable flight, the front wing is set at a slightly higher incidence (4°), so it carries more lift under normal cruise conditions and stalls first if the angle of attack becomes excessive. Combined with the nose-heavy condition this naturally dampens pitch oscillation like a conventional aircraft.

For smaller-scale prototypes, pitch, yaw and roll control for both vertical and fixed wing flight relies primarily on motor thrust vectoring—by varying RPM on different motors. For larger scale versions plans are to incorporate dedicated control surfaces (e.g.,

Elevons, flaperons) to enhance maneuverability and reduce reliance on high-thrust motor commands, especially at faster cruise speeds. We still aim to maintain thrust-vectoring redundancy: if control surfaces fail or are insufficient, the motors can still provide directional and roll authority, especially at near stall conditions.

CHAPTER 4

DETAILED DESIGN AND ANALYSIS

4.1 Aerodynamics

4.1.1 Methods and Tools

The aerodynamic design process relied on VSPAero, a vortex lattice / panel method tool integrated with OpenVSP (open-source parametric aircraft geometry tool developed by NASA), to estimate key performance parameters such as lift, drag, and pitching moments. For all the analysis in VSPAero, panel method was used, as it better captures the influence of the fuselage during iterations. These early studies allowed for quick iteration on wing sizing, airfoils, aspect ratios, and wing spacing before more resource-intensive simulations were performed. Once the general configuration was established, we performed a more detailed analysis based on our chosen propulsion systems (see section 4.2) and expected flight regime (400 feet ~ 120 m, standard atmospheric conditions) to evaluate interactions between the front and rear wings and to refine our understanding of flow patterns in both hover and forward-flight modes.

4.1.2 Trade Studies

Several airfoil profiles, including symmetrical, semi-symmetrical, and cambered airfoils, were considered in preliminary aerodynamic trade studies. Key performance metrics included lift-to-drag (L/D) ratio, stall characteristics, and ease of manufacturability.

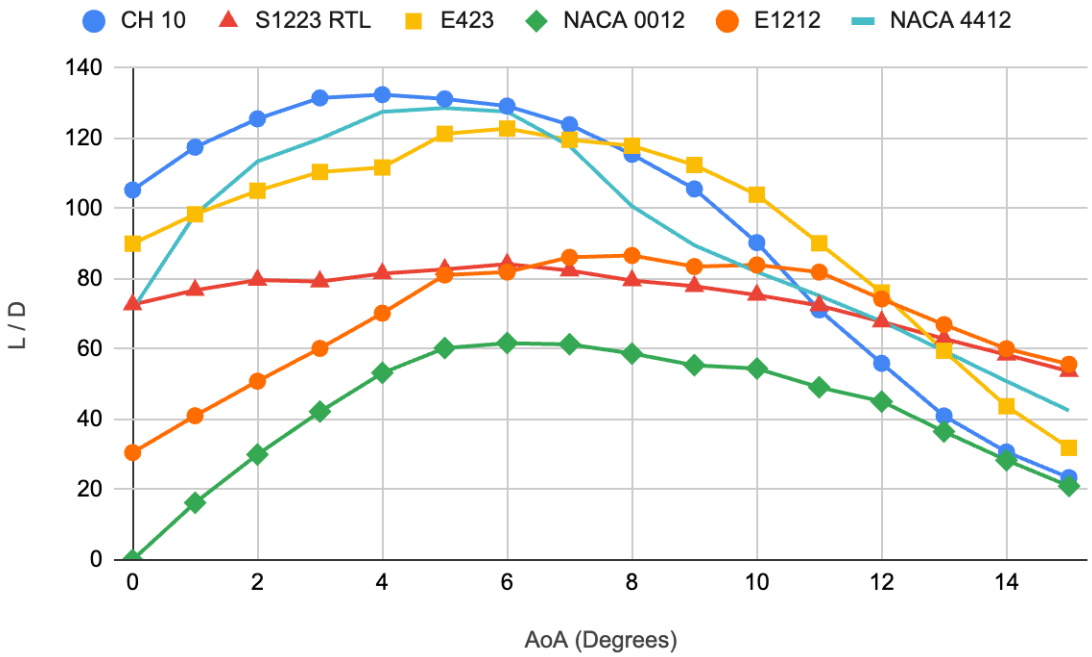

Figure 9: L/D as Function of Angle of Attack

Ultimately, the NACA 4412 airfoil was selected due to its favorable balance of aerodynamic performance—particularly a high L/D ratio at operating conditions—and ease of fabrication due to its well-documented geometry and simple, relatively thick shape. This airfoil provided comparable aerodynamic performance to more specialized high L/D airfoils while greatly simplifying the manufacturing process, a critical consideration given the use of additive manufacturing (3D printing) techniques and for manufacturing non 3D printed wings for scaled up aircrafts.

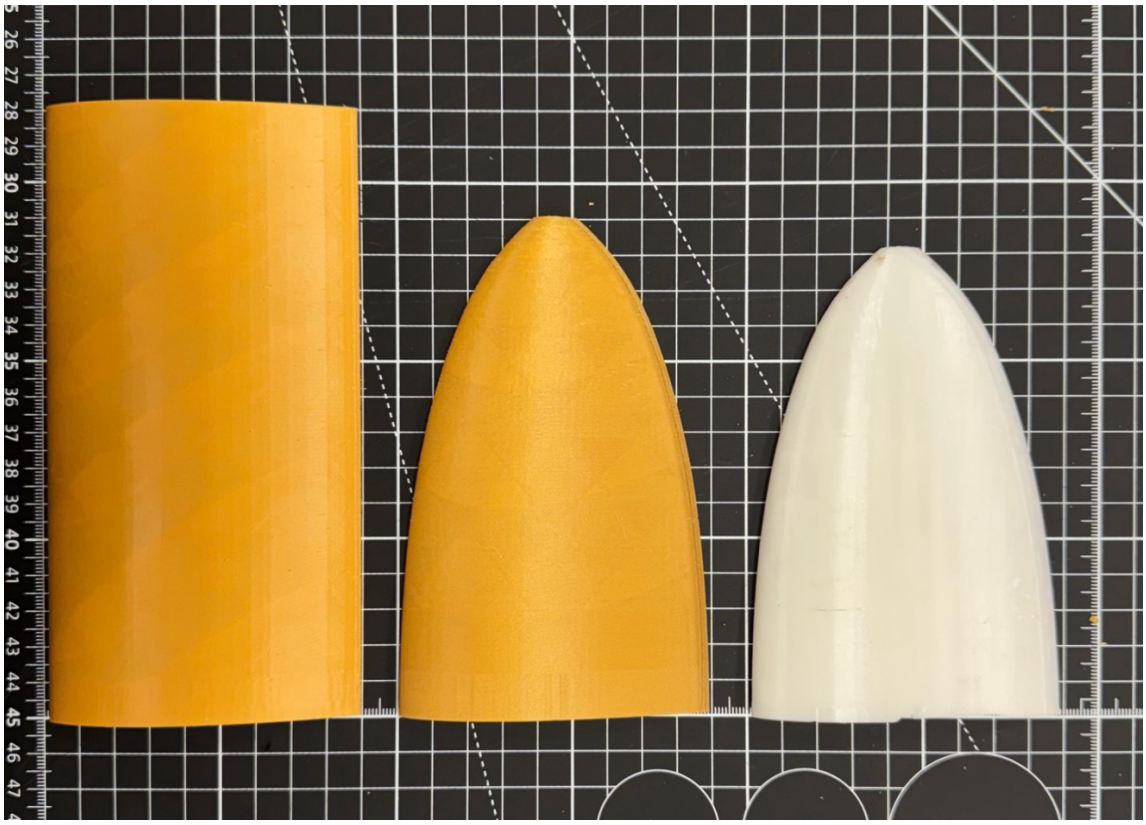

Figure 10: Wings with varying spans

Trade studies regarding wingspan and aspect ratio were conducted iteratively alongside prototyping efforts, with weight constraints playing a significant role in determining the feasible wing sizes. From propulsion system sizing (discussed in next section), we can estimate the wing area needed, from which aspect ratio of each wing was maximized in order improve efficiency. Initial analysis explored various aspect ratios to maximize aerodynamic efficiency; however, structural weight quickly became a limiting factor. Higher aspect ratios generally offer improved aerodynamic efficiency but at the cost of increased structural mass and complexity, negatively impacting hover performance and payload capability. The final wingspan and aspect ratio were thus chosen to strike a balance between aerodynamic efficiency, structural integrity, ease of manufacture, and

overall weight. Continuous prototyping allowed for practical assessments of how weight changes affected flight performance, guiding the decision toward a compact wing geometry suitable for the tandem wing tailsitter configuration.

4.1.3 Lift and Moment Characteristics

The UAV features a front inverted gull wing and a rear gull wing, each broken at a 45° angle (anhedral for the front, dihedral for the rear). Both wings use a NACA 4412 airfoil and have a 0.62 m span when projected tip-to-tip horizontally along with a nominal chord of about 0.09 m. The fuselage is compact, measuring 0.376 m in length. The front wing is set at 4° higher incidence relative to the rear to ensure balanced lift distribution about the center of gravity (CG), which is located at 0.12 m from the nose. This configuration targets a flight regime that includes vertical takeoff and landing (VTOL), as well as efficient forward flight. The angled (gull) wing sections also provide some vertical stabilizing surfaces in lieu of a dedicated vertical tail, while the tandem arrangement addresses center of gravity constraints for tailsitter operations.

The fully loaded mass of the aircraft is 1.5 kg, resulting in a weight $W = 1.5 \times 9.81$ $m/s^2 \approx 14.7$ N. The total lifting area S combines both wings. Estimating each wing's planform as $0.62m \times 0.09$ m ≈ 0.058 m^2, the total wing area across front and rear wings is approximately 0.116 m^2 which brings the wing loading to about 12.9 kg/m^2. The aircraft is designed to operate around 400 ft altitude, guided by the FAA limit for UAV operations, which can be approximated as standard sea-level conditions for this initial analysis (density $\rho \approx 1.18$ kg/m^3 near that altitude).

For level forward flight at speed V, the total lift L must balance the weight W. Thus:

$$L = W = \frac{1}{2}\rho V^2 S C_L \quad [1]$$

From preliminary analysis in VSPAero (using panel method), it was discovered that the aircraft had the best L/D ratio at CL = 0.5. Rearranging the above equation we get:

$$V^2 = \frac{2W}{\rho S C_L} \quad [2]$$

Plugging in $\rho = 1.18\ kg/m^3$, $W = 12.75\ N$, $C_L = 0.5$, $S = 0.116\ m^2$

$$V \approx 20\ m/s = 70\ km/h \quad [3]$$

Which is subsequently chosen as the cruise speed.

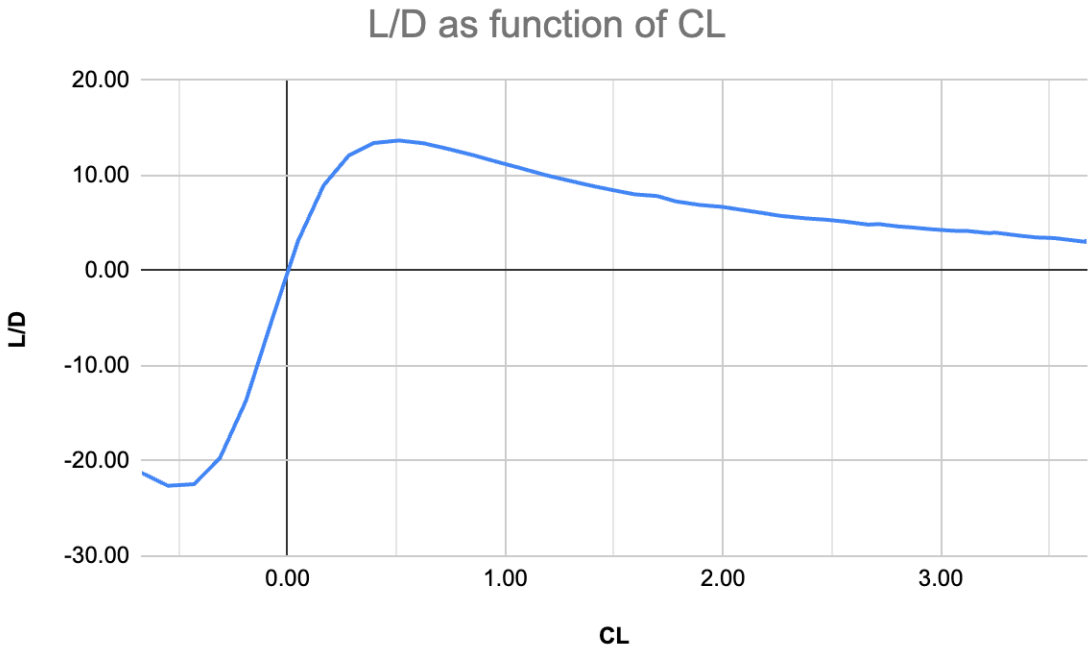

Figure 11: L/D as function of C_L

To calculate stall speed, we use $C_{L,\,Max}$ = 1.5 for NACA 4412 at a Reynolds number of 500,000 as maximizing C_L minimizes the velocity from the above equation:

$$V_{Stall} = \sqrt{\frac{2W}{\rho S C_{L,Max}}} = 11.38\, m/s \approx\ 41\, km/h \qquad [4]$$

4.1.4 Wing Incidence

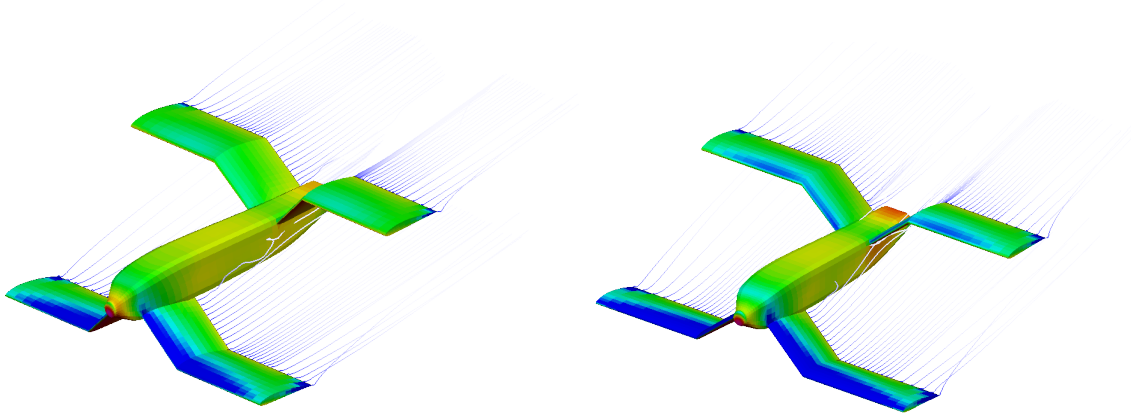

Figure 12: Front Wing Stalled While Rear Generates Lift

The front wing is set at an incidence of 4°, while the rear wing is set at 0°, ensuring the forward wing stalls first if the angle of attack is excessive. This approach drastically improves passive pitch stability (crucial for our case since the forward flight controller does not rely on any active stabilization) by relying on a nose-down pitching moment whenever the front wing approaches stall, similar to conventional airplanes. During VSPAero analysis, the case with CG at the geometric center of the aircraft and zero angle of incidence has a positive slope on C_{my} vs α indicating the aircraft is unstable in pitch. On the other hand, with the CG placed forward of the geometric center and the front wing

at a slight incidence, we get a negative slope (restoring moment when disturbed) on the C_{my} vs α graph as desired.

In steady cruise, the incidence offset also means the front wing carries a slightly larger share of lift at the trim AoA, while the rear wing carries less. Aerodynamically, this mimics a "reflex" configuration – the aft wing contributes a stabilizing nose-down moment similar to a tailplane lifting downward on a conventional aircraft.

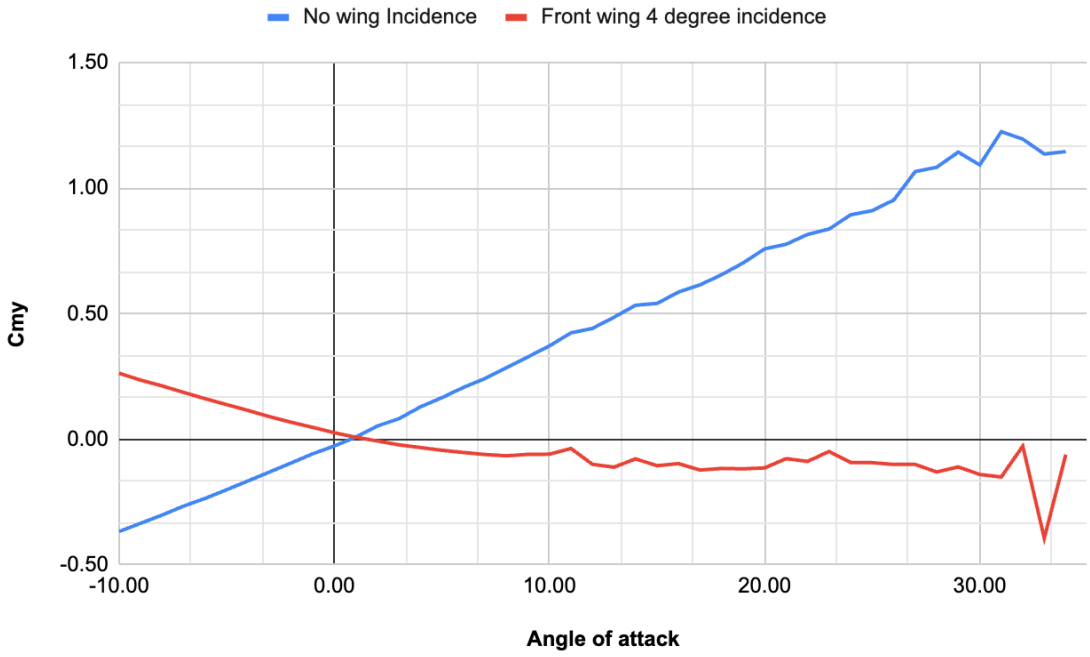

Figure 13: C_{my} as Function of Angle of Attack

4.1.5 Gull Angles

The gull and inverted gull wings on the aircraft are carefully designed to ensure the motors are placed equidistant from the CG while ensuring there is ample separation between the wings to minimize wing interference on the rear wing from the front wing. The span of the anhedral and dihedral sections of the front and rear wings were calculated

using the Volume coefficient method (Scholz, 2021) in order to provide lateral stability and natural roll damping.

$$C_V = \frac{2S_V \times L_V}{S_W \times b_w} \quad [5]$$

Where, S_V is the planform area of the vertical stabilizer, L_V is the moment arm from the airplane's center of gravity to the vertical stabilizer aerodynamic center, S_W = wing planform area and b_W is the wingspan. A common rule of thumb for the vertical tail volume coefficient, C_V, in small RC or light aircraft is anywhere from 0.02 to 0.04. Picking a $C_V = 0.3$ and rearranging the above equation for a conventional rear tail we get:

$$S_V = \frac{C_V \times S_W \times b_w}{2L_V} \quad [6]$$

where $S_W = 0.116$ m^2, $b_W = 0.62$ m and $L_V = 0.2$ m. Dividing this area between the rear V-tail geometry and accounting for the 45° angle the surfaces make with the fuselage we get a span of 8.4 cm for each of the planforms. Similarly, we get a span of 8.9 cm for each of the anhedral portions of the front wing. Essentially, the 45° canted wings "stand in" for a vertical tail by leveraging their projected area and dihedral geometry to keep the UAV pointed into the relative wind. This design choice simplifies the airframe (no separate tail surfaces) while still meeting stability requirements. It's worth noting that because the front wing's vertical area is ahead of the CG, excessive sideslip could introduce a small destabilizing moment. The design mitigates this by having a relatively high rear-area volume coupled with the larger moment arm relative to CG.

Based on these refinements a stability analysis with VSPAero was conducted to get the eigenvalues for Phugoid, Dutch Roll, Roll and Short period. Further analysis on the Cooper Harper scale, which rates aircraft stability on scale of 1 to 9 with 1 being ideal, revealed that the aircraft exhibits level 1 stability for all modes.

Mode	Eigenvalue	Requirement for Level 1
Phugoid	0.07	$\zeta > 0.04$
Roll	0.3	$\tau < 1$ s
Dutch Roll	$\zeta = 0.29$ $\omega = 3$ rad/s $\zeta\omega = 0.5$ rad/s	$\zeta > 0.19$ $\omega > 1$ rad/s $\zeta\omega > 0.35$ rad/s
Short Period	0.56	$0.35 < \zeta < 1.3$

Table 2 – Stability Derivatives for Cooper Harper Scale Level 1 Requirement Criteria

4.2 Propulsion System Sizing

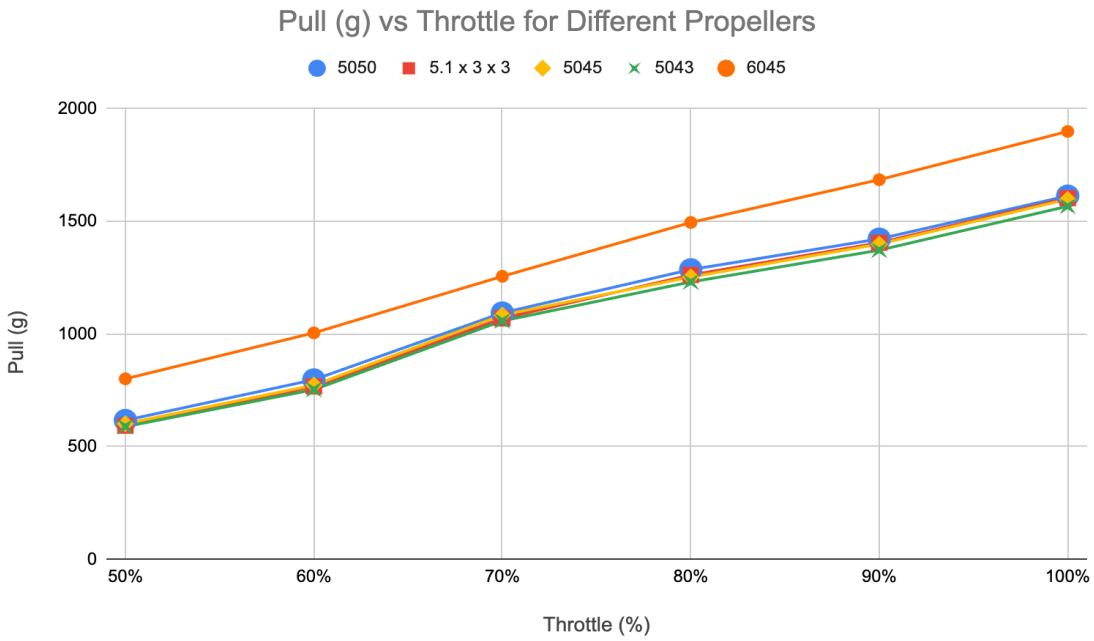

Figure 14: Thrust as Function of Throttle

In general quadrotors shoot for a minimum 2:1 thrust to weight ratio (T/W) while airplanes, especially long-range load carrying class, have a T/W = 0.5-1. For an initial mass estimate of 1.5 kg (not including battery and motors which would have a mass of about 500 gm) a propulsion system is required to provide approximately 40 N (4 kg) of thrust to meet the 2:1 T/W ratio needed for effective vertical flight control. In order to account for propulsion inefficiencies and lack of dynamic thrust test data available for most of the propeller/motor combinations out there a safety factor of 1.5 was chosen. Subsequently the maximum total required thrust from all four motors was calculated to be 60 N (6 kg). Based on the thrust requirement, iFlight's Xing 2207 1800 KV along with three bladed, 5.1-inch diameter 3-inch pitch propellers.

This selection prioritizes forward-flight efficiency over hover efficiency, which is acceptable since the mission involves quick vertical takeoffs/transitions but longer cruise segments. A 3-inch pitch means that in one revolution the propeller would advance 3″ (7.62 cm) through the air if it had 100% efficiency. This is a relatively *coarse* pitch for a 5″ prop, chosen to favor forward flight performance. In forward flight at ~20 m/s, a finer-pitch prop would start to "windmill" (air driving the prop) or operate at negative angles of attack, causing drag. The 5×3 prop, however, can still produce thrust at 20 m/s airspeed when spinning near its design RPM.

Essentially, the high pitch allows the prop to act like a proper airplane propeller during cruise, generating thrust instead of spinning idly. This improves propulsion efficiency in forward flight – the motors can unload (draw very little power) yet keep the prop spinning enough to offset its drag. By contrast, a low-pitch prop would become

inefficient at forward speed and create more drag or require higher RPM to “bite” the air. (This configuration is akin to racing quadcopters, which use small, high-pitch tri-blades to achieve high speeds and agile acceleration.) Using the drag polar from Section 4.1, we estimated the thrust needed in cruise and the power required. At the cruise speed ~20 m/s, the total drag is about 1.9 N. This is extremely small compared to the hover thrust (~30 N); it implies that in wing-borne flight, only ~2 N of thrust is needed to maintain level cruise. Even accounting for some additional drag from the fuselage and props, say the total drag is 3–5 N, each of the four motors only needs to produce ~1 N (0.1 kgf) of thrust in cruise – essentially idle throttle. The power P = T x V to overcome 2.5 N drag at 20 m/s is only 50 W. With propeller efficiency around 0.7 in cruise, the electrical power per motor is on the order of 20 W. This indicates that cruise flight is very power-efficient for this design (a common feature of VTOL UAVs: wing-borne flight consumes far less power than rotor-borne hover).

By incorporating the masses of the motors and battery, along with their predicted performance into the calculations, the range and endurance estimates were gathered. A MATLAB code was written to iterate over different battery sizes and subsequent final weight estimates to obtain total weight, range, and velocity to maintain level flight as a function of battery size. A correction factor of 0.25 times the battery weight (calculated based on weight and battery capacity–gram/mAh for 6 cell 22.4 V batteries) was added to the weight of the UAV to account for additional structural reinforcement that might be needed. Moreover, the code uses thrust data from the manufacturer to estimate the power during the hover phase (20-30% of the flight). During the iterations, for forward flight, C_L = 0.5 was held constant to achieve the cleanest configuration possible. Using the weight

estimate of the battery and airframe combined along with the constant C_L, cruise speed was calculated using equation [2] and Cd was calculated using the Oswald's efficiency based drag polar equation:

$$C_d = C_{D0} + \frac{{C_L}^2}{2\pi \times AR \times e} \quad [7]$$

Where C_{d0} = 0.05 from VSPAero, Aspect Ratio AR = 6.88 and e = 0.8 (typical for UAVs with multiple lifting surfaces inefficiencies) were used. There is an additional two in the denominator of the induced drag term, due to the tandem wing layout. Even though the aircraft's front wing is at a slight incidence, due to the relatively small difference in moment arms the lift distribution can be assumed as being equal due to the large CG range of the tandem wing configuration. Moreover, since both wings stall before the front wing's airflow can interfere with the rear wing, we can safely disregard the contribution of interference drag during fixed wing flight.

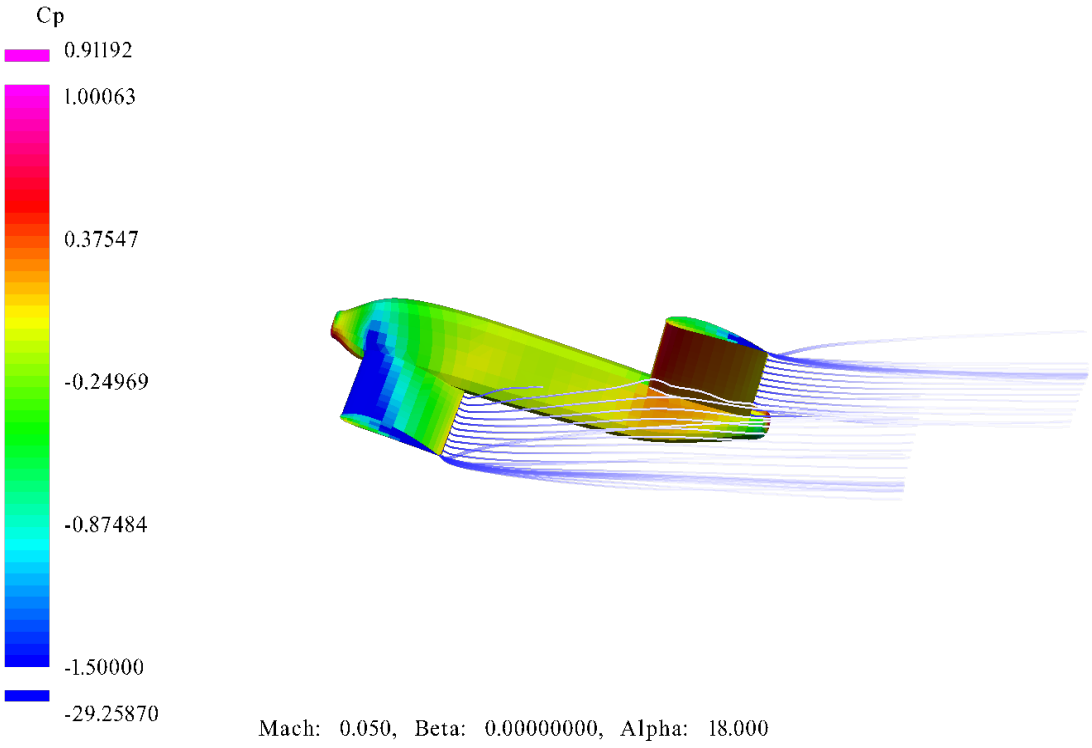

Figure 15: Front Wing Stalls Before Airflow Interferes with Rear Wing

Based off the calculated C_d, drag force and hence the required thrust is calculated as follows:

$$T = D = \frac{1}{2}\rho V^2 S C_d \quad [8]$$

Power consumption at the needed thrust is then calculated based on thrust data for the motor/propeller combination.

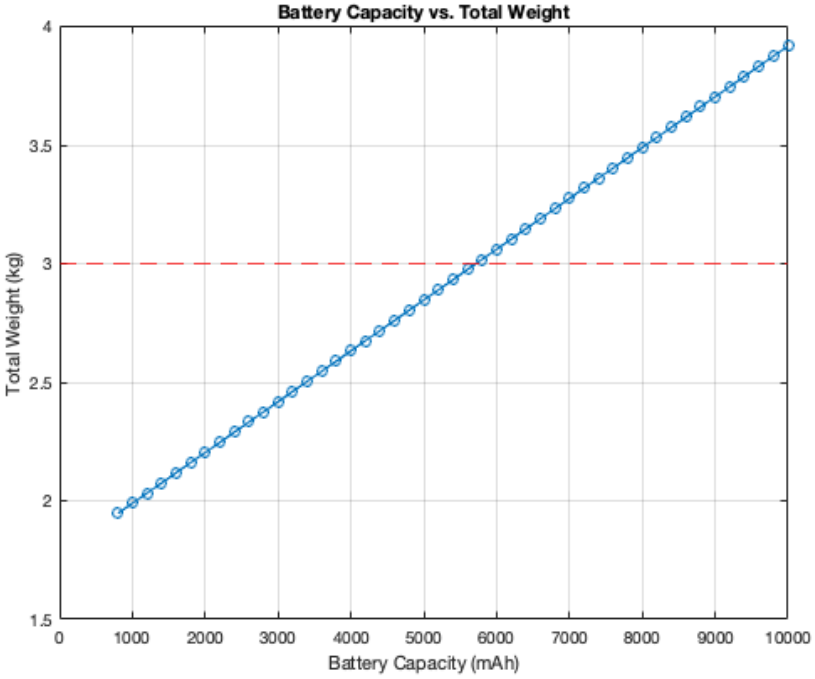

Figure 16: Total weight as a function of battery capacity

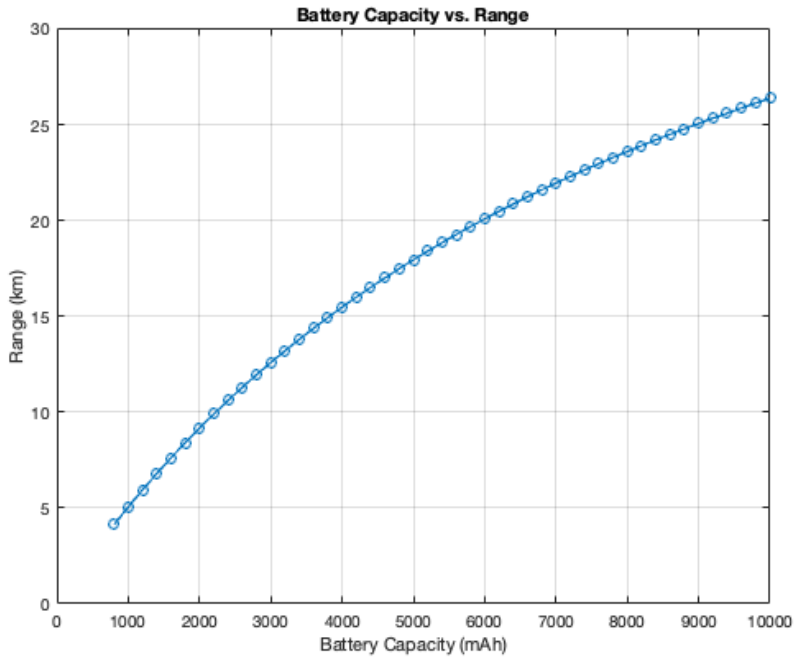

Figure 17: Range as a function of battery capacity

4.3 Structures

4.3.1 Design Approach and Material Selection

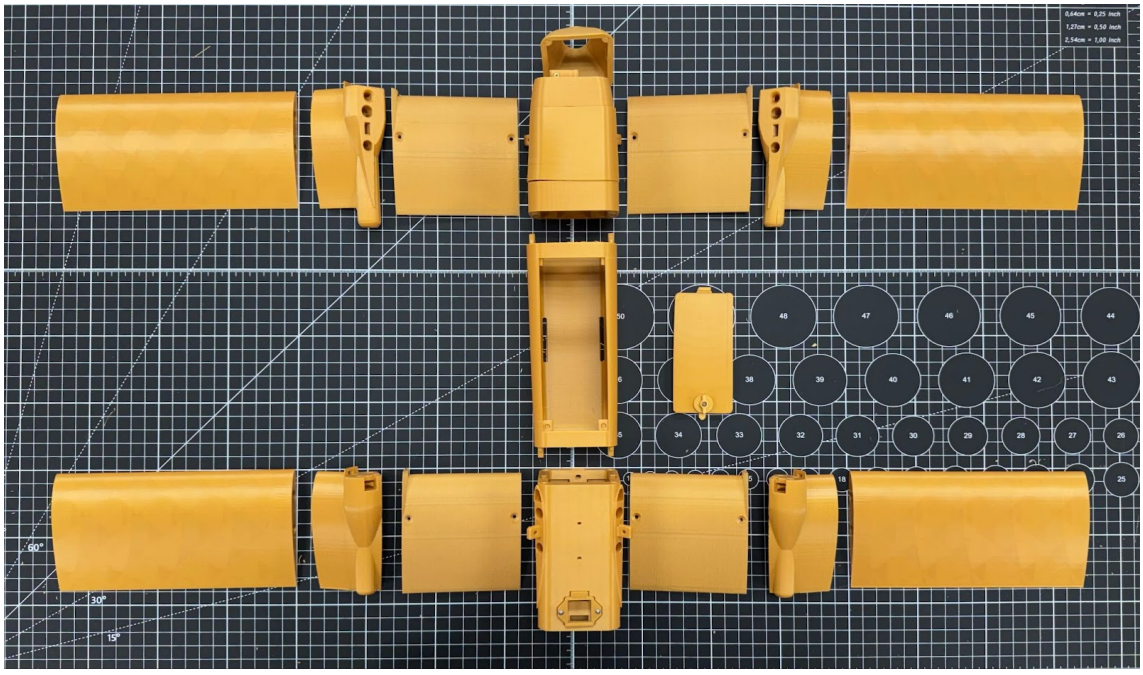

Figure 18: 3D Printed Components of the UAV

The airframe was fabricated using fused deposition modeling (FDM) 3D printing, a choice driven by its rapid prototyping capability and low cost for complex geometries (Šančić et al., 2023). FDM enabled a modular design: the UAV's wings, fuselage sections, and motor mounts were printed as interlocking modules. This modularity accelerates iteration and repair – damaged sections can be reprinted and replaced individually, reducing downtime. The use of 3D printing also allowed integration of features like snap-fit joints and internal conduits that would be costly and time consuming to achieve with traditional fabrication. Another advantage of this approach is that wing sets with different spans can be printed for different mission profiles: longer

span wings for carrying smaller payload for longer distances at lower speed, or smaller span wings for carrying larger payload shorter distances at higher speeds. Given that the cost of printing a set of wings (each set consists of four wings and refer to the flat portion of the planforms) is approximately $3.00, having multiple wing sets doesn't add significantly to the costs.

While FDM parts have anisotropic mechanical properties (weaker strength in the build direction) (Šančić et al., 2023), the design mitigated this by ensuring critical load bearing components had additional reinforcement in the form of light weight carbon fiber tubes aligned with the build direction. For example, wing sections were designed and printed such that layer lines loop around the airfoil to ensure clean wing geometry, while the build direction (span of the wing) is reinforced with internal carbon fiber tubes better withstand bending along the wingspan.

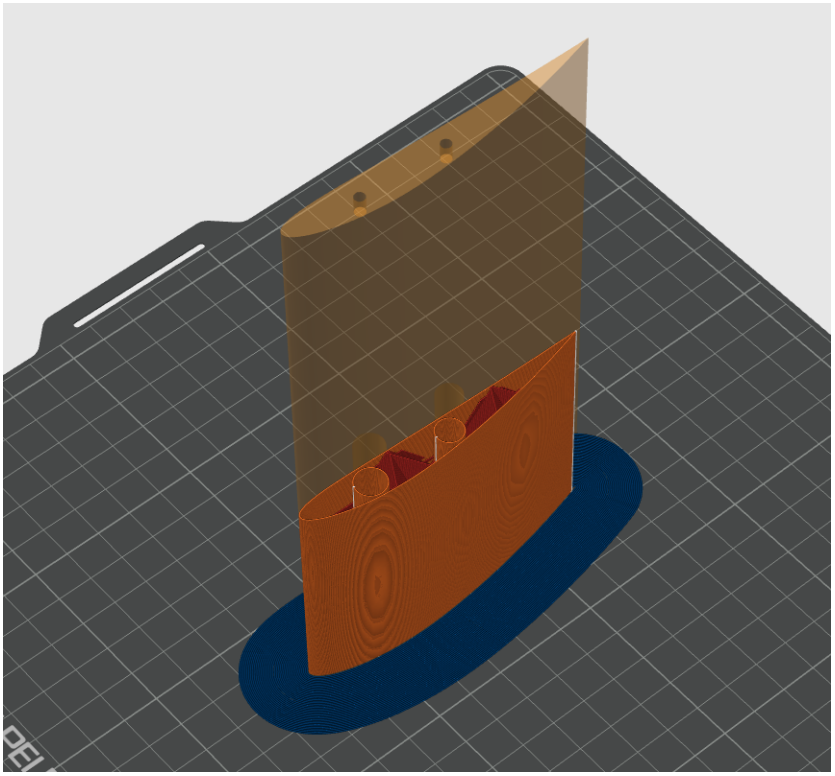

Figure 19: Wing End in 3D printer's Slicer Software.

PETG (polyethylene terephthalate glycol) filament was chosen over alternatives like PLA or ABS. PETG offers a good balance of strength and ductility; although its tensile strength is slightly lower than PLA's under similar print settings, it is far less brittle and maintains integrity under higher temperatures (Šančić et al., 2023)This is crucial for an outdoor UAV, as PETG parts will not soften or deform under sun-heating or motor heat as PLA potentially could. PETG's chemical resistance is an added benefit for exposure to fuel residue or rain. The slight reduction in strength was deemed acceptable given the UAV's safety factors and the ability to compensate via design (thicker walls or reinforcement).

4.3.2 Wing Design

The wings were primarily evaluated for forward-flight conditions since in hover, the primary loads concentrated near the motor mounts (due to thrust and yaw torque). In forward flight, the wings were expected to experience classic lift-induced bending and torsional loads, especially near the gull "kink" angles and the root. When designing a quadrotor, the arms that the motors mount on are kept as stiff as possible to minimize any oscillations and vibrations from the torque generated by the motors, which can "confuse" the flight controller especially in stabilized mode. Thus, in order to maximize the stiffness of the anhedral/dihedral sections of the wings (which form the motor arms in this case and the root for the flat portion of the wings) are 3D printed with slightly higher infill of about 8% (when compared to flat sections of the wing which have an infill of 5%).

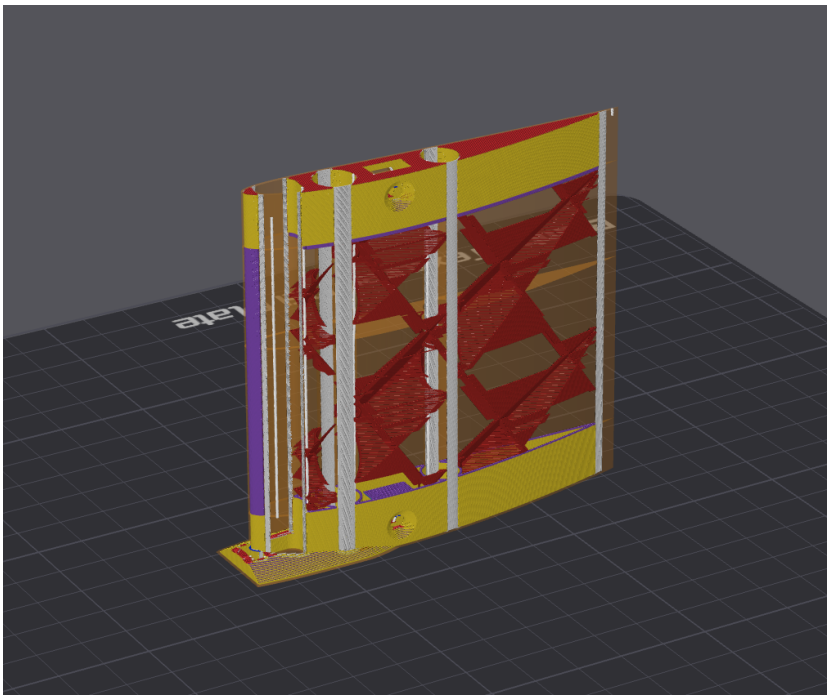

Figure 20: Anhedral Section of Front Wing.

Moreover, variable layer infill and well thickness were used to selectively add strength at either ends of these wing mid sections to account for the mounting hole and added stress during assembly/disassembly of the aircraft. Two carbon spars, one 8 mm diameter and the other 7 mm, run through the length of these sections and attach to the fuselage one end and the motor pods/mounts on the other. This ensures the structure is lightweight yet stiff, meeting the design goals.

To validate the wing stiffness, a simple 3-point bending test was conducted on a wing half-span: clamped at the root and loaded at the tip with weights until failure. The deflections were measured and compared wing loading expectations from aerodynamic analysis from section 4.1.

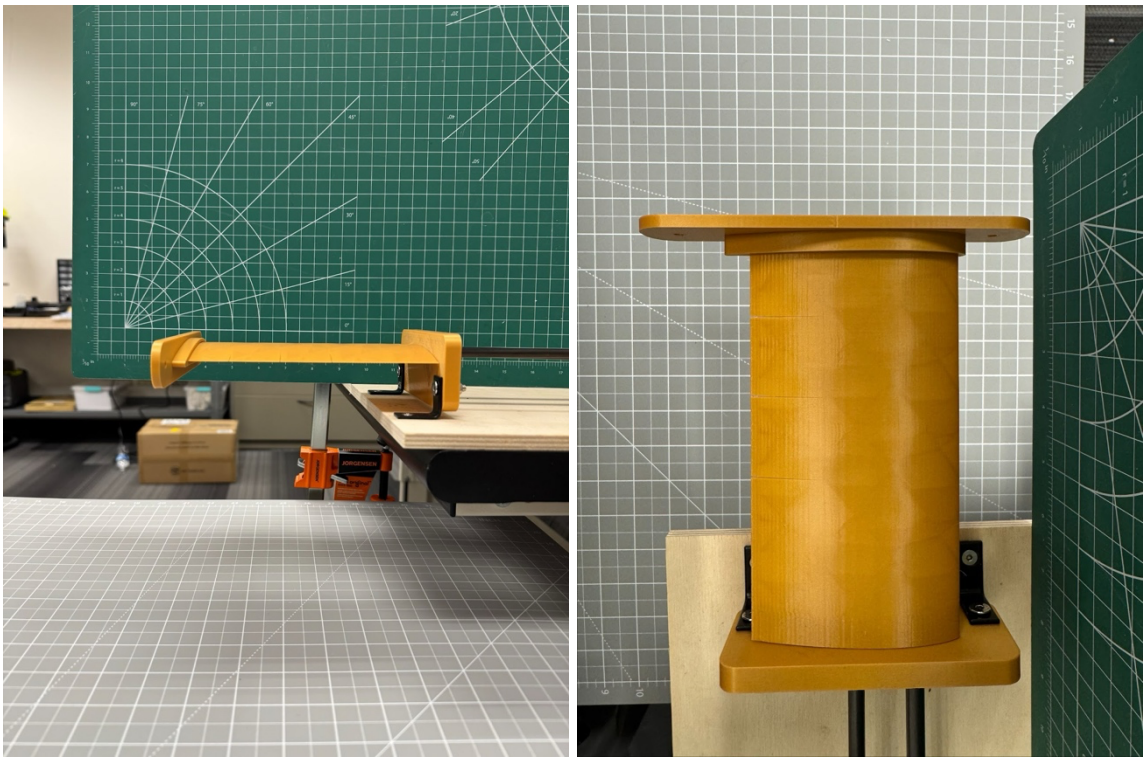

Figure 21: Wing Testing Setup

No structural failure was observed up to 150% of the maximum expected flight load for the final iteration of the wing. Furthermore, the wing's torsional rigidity benefited from the closed-section airfoil shape of the printed skin. Even though FDM layer interfaces could act as potential shear failure planes, the continuous perimeter shells and spar integration provided sufficient torsional support for resisting flutter and twist at cruise speeds.

4.3.3 Fuselage Design

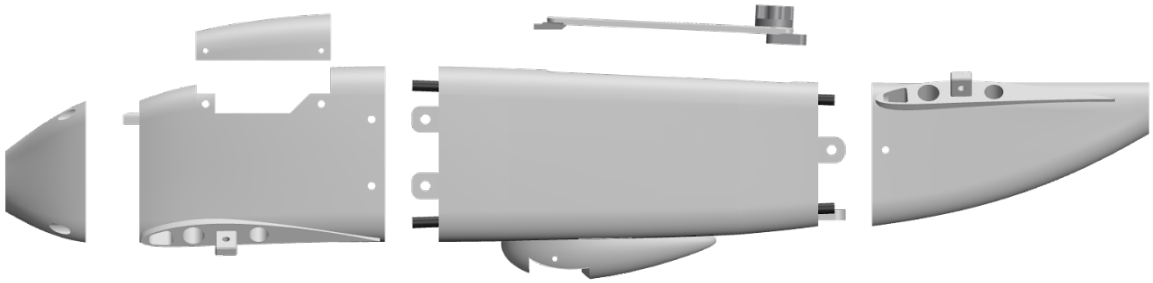

Figure 22: Exploded View of Fuselage

The fuselage is split into a nose cone and three main modular sections that use heat set inserts and M3 bolts to connect to each other. Front section contains the avionics bay and attaches to the front wing, the center section houses the battery, and the rear section attaches to the rear wing. By placing the avionics in the front section, the desired CG of 12 cm from the nose is achieved. The front and rear sections have walls that are 0.8 mm thick for the most part while sections where the wing attaches, the walls are much thicker and hence have 15% infill to ensure the parts are strong but not too heavy.

The fuselage is split into a nose cone and three main modular sections that use heat set inserts and M3 bolts to connect to each other. Front section contains the avionics bay and attaches to the front wing, the center section houses the battery, and the rear section attaches to the rear wing. By placing the avionics in the front section, the desired CG of 12 cm from the nose is achieved. The front and rear sections have walls that are 0.8 mm thick for the most part while sections where the wing attaches, the walls are

much thicker and hence have 15% infill to ensure the parts are strong but not too heavy. Center section of the fuselage has 0.8 mm thick walls as well except for where there are ribs, to ensure the part is printed without any support material.

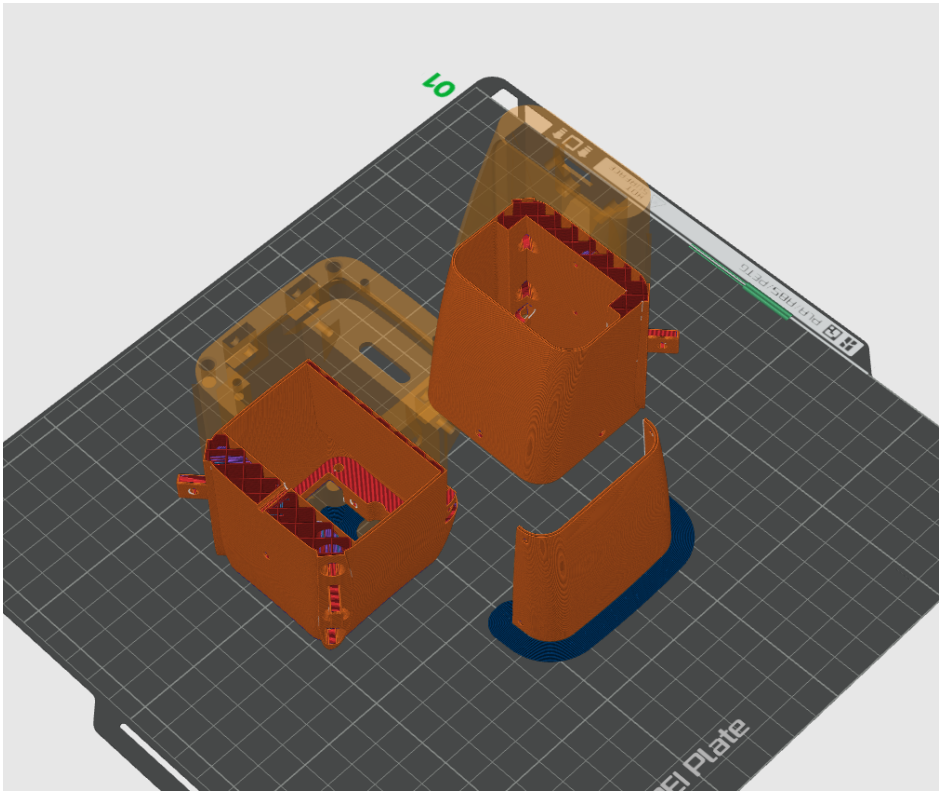

Figure 23: Fuselage Sections in 3D Printer's Slicer Software

Adding support material increases model print time, filament used, causes stringing in materials like PETG, compromising strength and overall quality of the part especially when working with such thin walls. Therefore, instead of an abrupt change in the cross section of the fuselage, the ribs are added in a gradient (45° angle from the build axis) which avoids the overhang that would come from a traditional flat rib. The decision to add ribs was made during testing as torsional issues were discovered in the fuselage due

to the presence of a large opening for access to the battery compartment coupled with the fact that the fuselage sections are printed layer by layer along its length. Due to the inconsistencies with which the 3D printing slicer software generates infill for a part, running FEA simulation for different situations wasn't feasible since any results couldn't be trusted due to the anisotropic nature of the printed part (for FDM printed parts the strength of the part in XY plane is >> XZ, YZ). To assess this, a test jig was built: one end of a fuselage section was clamped, and a known torque was applied to the other end via a lever arm. The resulting twist (in degrees per Newton-meter) was measured. This experiment revealed that the initial fuselage design (with widely spaced ribs and large open bays) had a relatively low torsional stiffness, primarily limited by shear deformation in the thin skin between ribs.

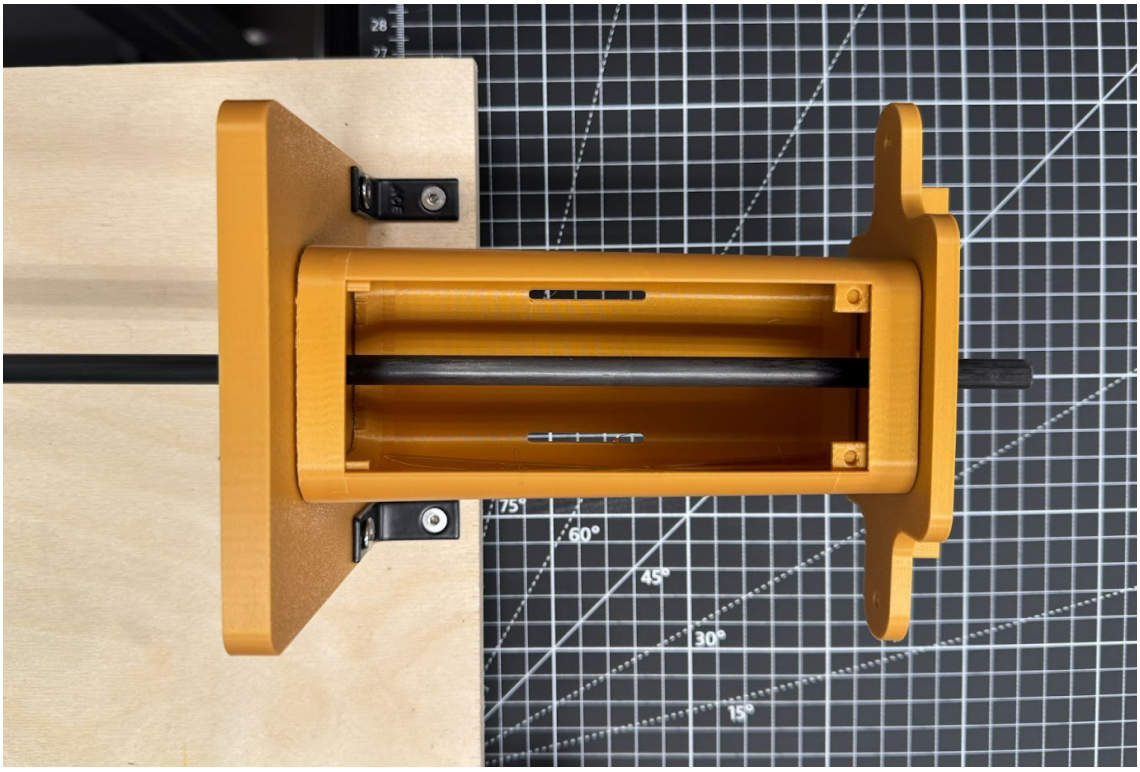

Figure 24: Fuselage Torsional Testing Setup

In response, the design was modified to include an internal shear web running diagonally along the sidewalls (a thin lattice-like structure printed inside the fuselage walls in the mid-span bay). This web, essentially forming a Warren truss pattern on the fuselage interior, reduced the measured twist by ~20%. Further iteration resulted in the final design which resembles traditional fuselage designs with ribs, four 4mm spars and skin. However, the skin and the ribs are printed as one piece. The 4mm spars run through the length of the center section and connect to the front and rear sections of the fuselage. When compared to the original design, the new fuselage weighs only 15 grams more. Overall, the fuselage's combination of tuned skin thickness, thoughtfully placed ribs, and added shear webs provided a stiff but lightweight structure.

4.3.4 Motor Mount Integration

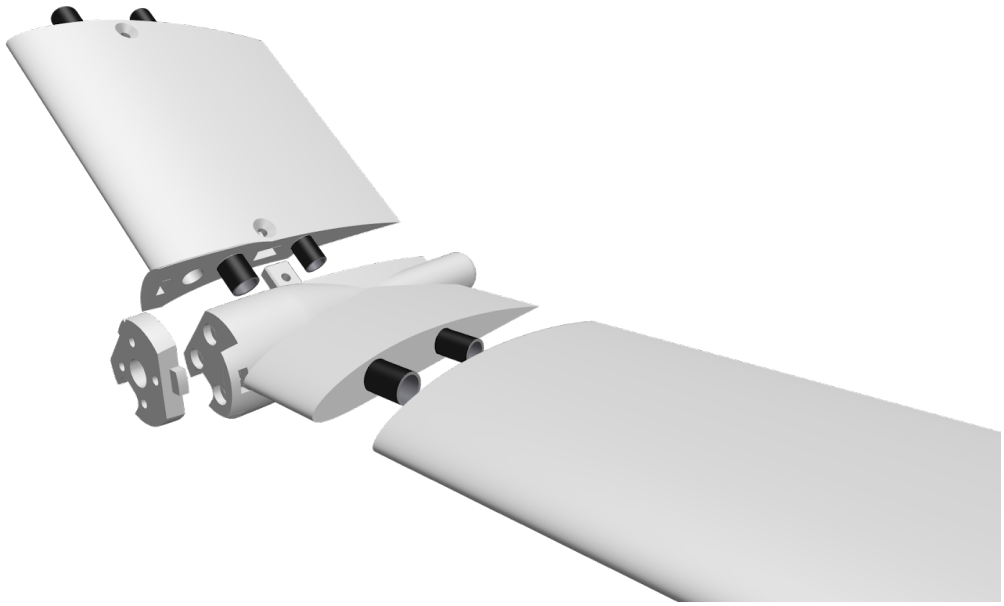

Figure 25: Front Left Wing Exploded View

The motors were located at the gull "kinks," where dihedral or anhedral angles met. This placement naturally introduced torque from thrust vectoring and while transferring the bending moment from the rest of the wing. The motor mounts were given special design attention because they must withstand high thrust forces, motor torque, and occasional impact loads (in a tailsitter configuration, a rough landing can directly stress the motor mounts). Each motor is affixed to a 3D printed mount bracket that interfaces between the motor and the wing structure. These mounts were printed in PETG with 100% infill for maximum strength around the screw holes. To handle the motor torque (reaction torque from the spinning propeller), the layer orientation was chosen such that the layers run perpendicular to the plane of rotation – this means the shear from torque is carried by intralayer filament instead of weaker layer bonds.

For crash resilience, the interface between the mount and wing has a mechanical fuse: a narrow neck that will intentionally snap off under extreme impact, isolating the motor and wing from further catastrophic damage. This was verified by drop-testing the mounting geometry with dummy weight from a moderate height – the mounts plastically deformed or cracked at the designed points, absorbing energy that otherwise could have splintered the wing or caused damage to the motor.

CHAPTER 5

AVIONICS AND FLIGHT CONTROL ARCHITECTURE

5.1 Avionics

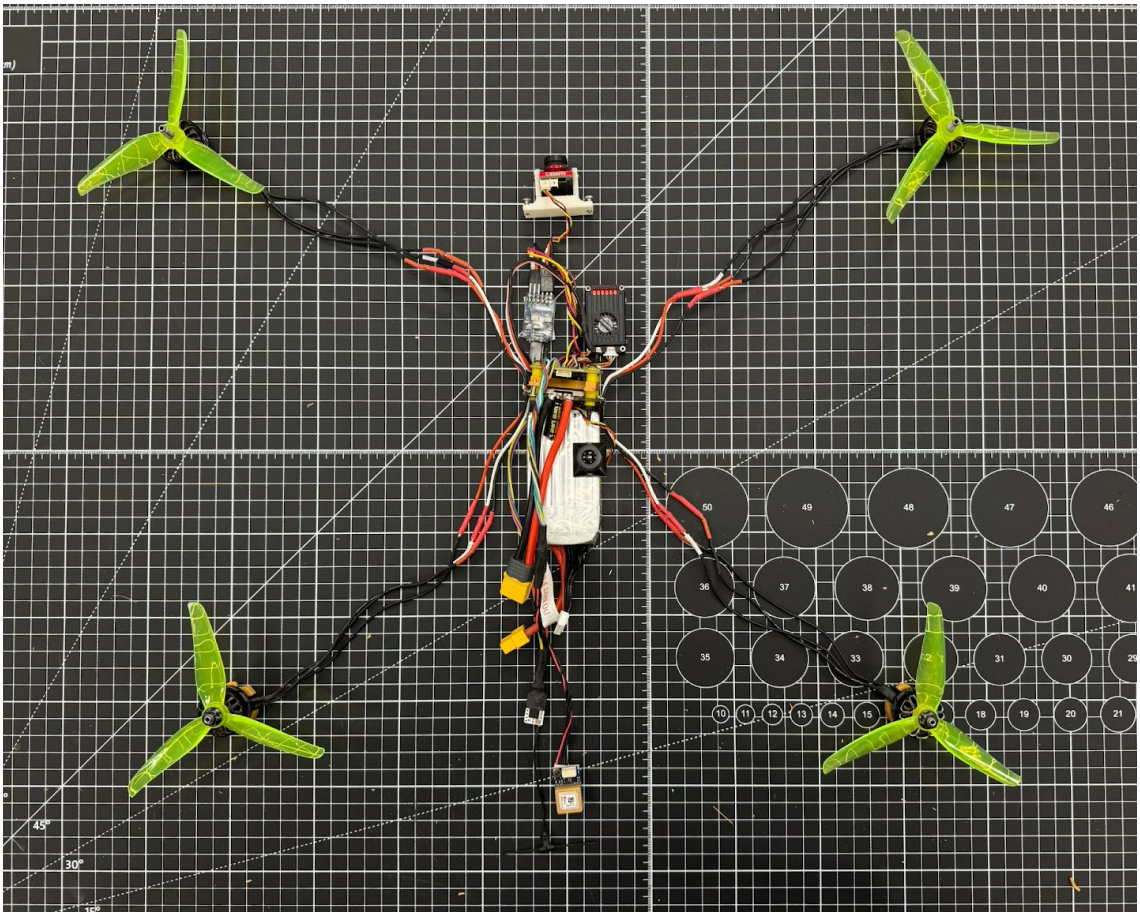

Figure 26: Avionics Architecture

The UAV is equipped with a comprehensive avionics suite centered on a modern flight controller board. The flight controller is a STM32-based autopilot board running the Betaflight firmware (see §5.2), which provides the primary inertial measurement unit (IMU) and control logic. This board includes a 3-axis gyroscope and 3-axis

accelerometer for attitude and angular rate sensing, a magnetometer for heading, and a barometric altimeter for altitude estimation. The IMU feeds high-rate orientation data to the flight control algorithms, while the barometer enables altitude hold modes by measuring atmospheric pressure. An external GPS module is also integrated, interfaced via UART to the flight controller. The GPS provides real-time latitude/longitude and ground speed, which were used mainly for logging and for potential future autonomous navigation (e.g. return-to-home or position hold functionality).

For command and telemetry, the UAV uses a dual communication link: a 2.4 GHz RC radio link for primary flight control inputs, and a secondary First-Person Video (FPV) link. The RC link consists of a standard transmitter/receiver pair (FrSky - TBS Crossfire), which outputs PWM signals to the flight controller corresponding to pilot stick commands. The UAV is also outfitted with a 5.8 GHz FPV video system: two micro FPV cameras, one in the nose and one in the belly, feed a video transmitter, allowing the pilot to view a first-person perspective during both vertical and forward flight modes. This was particularly useful during transition testing, as the pilot could quickly switch between cameras to maintain situational awareness during different flight regimes.

All components are powered through a power distribution board linked to the main battery. A 5 V regulator on the flight controller powers the receiver and other peripherals, while the FPV transmitter has its own filtered regulator to prevent motor noise from affecting the video feed. The avionics components are

placed to minimize electromagnetic interference: for example, the GPS/magnetometer unit is mounted on the tail, away from high-current wires and the motors, reducing magnetic distortion and GPS multipath interference. The internal layout ensures that the IMU is in line with the vehicle's center of gravity (to reduce acceleration errors) and isolated with silicone pads to dampen high-frequency vibration from the motors. Vibration levels encountered in hover (per the flight controller's on board sensors) were within acceptable ranges, so no additional mechanical isolation was needed.

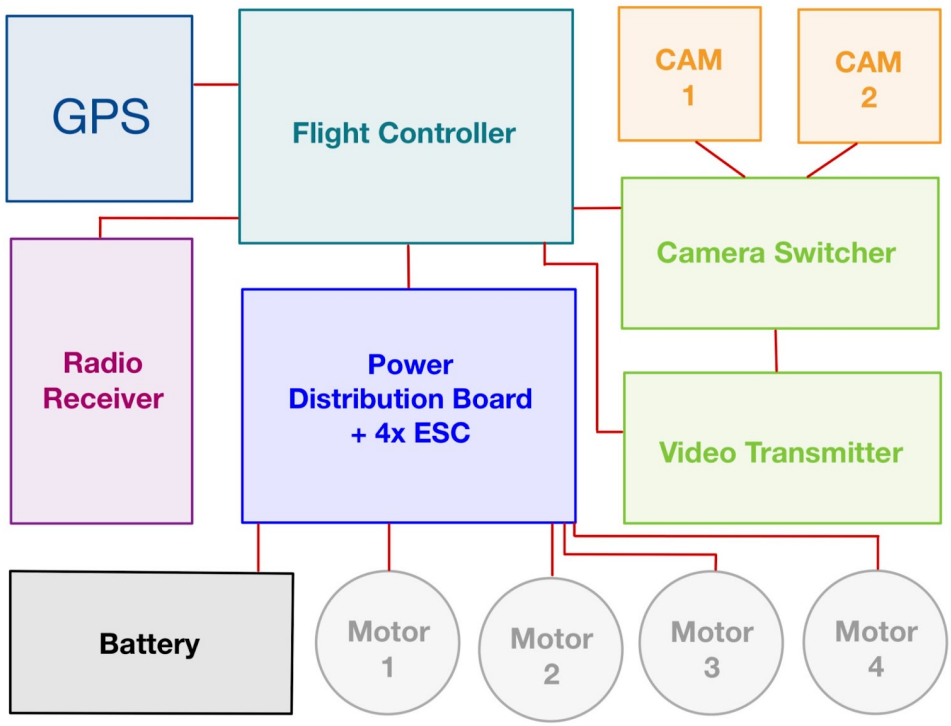

Figure 27: Avionics Architecture Components

In operation, these avionics components work together as follows: The flight controller reads sensor inputs (IMU, barometer, etc.) and computes stabilizing outputs to the motors at a high update rate. It mixes pilot commands (set points) with stabilization inputs (error correction) to drive the electronic speed controllers (ESCs) of the motors. The GPS data was recorded to evaluate hover drift and ground speed during forward flight and is intended for later use in autonomous modes. The pilot's RC commands can also toggle flight modes on the controller (for example, switching between a stabilized hover mode and manual acrobatic mode for transitions). A real-time on-screen display (OSD) overlay is transmitted over the FPV video, showing critical telemetry such as battery voltage, altitude, and attitude indicators. This OSD, generated by the flight controller, helped the pilot maintain situational awareness, especially when the UAV was high or far enough that orientation cues were hard to see directly.

Overall, the avionics stack is similar in spirit to those of other experimental UAVs, albeit using a smaller flight controller typical of hobby drones rather than a full-sized autopilot. Each component in the stack has a clearly defined role: the flight controller for real-time control, the GPS for global positioning, the FPV for visual feedback, and the RC link for pilot input – integrated to function reliably as a whole.

5. 2 Flight Control Firmware (Betaflight) and Customization for Tailsitter

The flight controller runs Betaflight, an open-source flight control firmware known for its high performance on smaller flight controllers. Betaflight does not natively have a "VTOL" mode, but it allows manual adjustment of the board orientation and channel mixing. By contrast, full-feature autopilots offer sophisticated waypoint navigation and transition handling but come with greater complexity and require resource intensive hardware. Given that forward flight testing could be done under manual RC control (since aircraft is passively stable in forward flight), Betaflight provided a simpler platform on which to build the custom VTOL control logic. For control in vertical flight, no modification to the standard "X" frame quadrotor controller is needed. In a stabilized mode, with correct PID tuning, the aircraft hovers just like a quad rotor. Even though the motors are offset in the Z axis (assuming in vertical flight x-axis points forward and z-axis is up (in line with the fuselage)), the moment arms about the CG are the same since in vertical flight CG is precisely in middle of the fuselage (or centroid of the 4 motors when looked from top down), hence demonstrating the advantage of tailsitter and tandem wing configuration, we can have the optimum CG placement for both flight modes without needing to place motors far out from the wings.

To support the tailsitter, a key customization was the use of Betaflight's adjustment channel feature to alter PID gains based on a logic switch for flight mode. For example, in hover (vertical flight mode) we used a set of gains tuned for multirotor-like control (very responsive yaw authority via differential thrust, etc.), whereas for forward flight we switched to a different gain profile that assumes a stable aircraft requiring less

yaw authority from motors. Essentially, we treated Betaflight's "rate profile" as a means to have two sets of PID values: one optimized for hover and one for cruise. This is not an out-of-the-box solution for UAVs but was possible through Betaflight's command line interface and Lua scripting on the RC transmitter.

5.3 Control Strategies for Transition

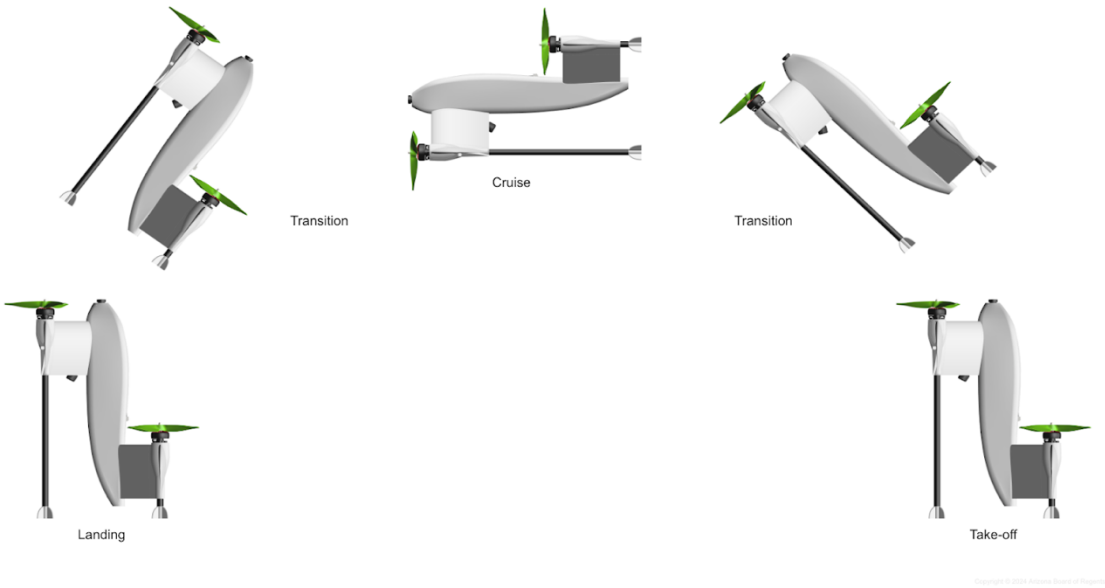

Figure 28: Tandem Wing Aircraft Flight Cycle

In order to transition from vertical to forward flight, the pilot increases throttle to gain altitude and airspeed while pitching the nose forward, as the wings start generating lift and the aircraft is approximately 30◦ from the horizontal, the pilot flips a switch on the radio controller that switch the roll and yaw axis on the controller to account for the switched axis on the aircraft and also turn off active stabilization (manual/acro mode).

Our Betaflight setup being in acro mode means the controller always interprets inputs in the vehicle's body frame (relative to its current orientation). Thus, as the vehicle transitions, there isn't an abrupt switch in the firmware; instead, the pilot's stick input that was controlling yaw in hover naturally begins to induce a banking motion as the vehicle approaches horizontal (switching of the yaw and roll axes). In forward flight, the aircraft is passively stable and thus controllable without the need for active stabilization. For future scaled up versions, the plan is to run all motors at constant RPMs and use control surfaces on the wings to maneuver in forward flight (potentially adding redundancy, since if a control surface or a motor gives out the other set can still handle the aircraft at least in forward flight.). For landing, the aircraft goes in a nose up attitude as the pilot decreases the throttle and turns on the stabilization while swapping back the yaw and roll controls on the controller (going back into vertical flight mode). Once the craft is stabilized, the pilot lands it as he would with any standard quadrotor.

It is recognized that a more robust solution in future is to implement an automatic yaw-roll blending. For example, more sophisticated autopilots like ArduPilot's tailsitter controller uses a blending factor to swap differential thrust from controlling yaw (in hover) to controlling roll (in plane mode) as airspeed builds (*Ardupilot Tailsitter Planes — Plane documentation*, n.d.).

CHAPTER 6

TESTING

6.1 Ground Test Setup and Methodology

Figure 29: Prototype with FPV Goggles and RC Transmitter

Before free-flight testing, a series of tethered hover trials were conducted to safely tune the flight control PID loops. The UAV was secured to a soft elastic tether anchored to the ground – long enough to allow vertical takeoff to ~2 m height but preventing it from

drifting or tipping over completely. The tether provided a safety margin while we dialed in the controller gains. We followed a methodical four-step tuning sequence corresponding to the cascaded control loops (from innermost rate control to outermost position control):

Rate Controller Tuning:

The innermost loop controls the angular velocity (roll, pitch, yaw rates) using gyro feedback. We began by setting very conservative gains and then incrementally increased the rate PIDs. For example, we introduced a small oscillatory yaw input (by quickly twisting the vehicle by hand on the tether) to see if the yaw rate controller would damp it. Over successive trials, the P gain for yaw was raised until a slight overshoot was observed, then backed off to ensure stability. A similar approach was done for pitch and roll rate—though roll rate in our case was less directly observable due to the tether and tandem configuration.

Attitude (Angle) Controller Tuning:

With the rate loops stable, we enabled the outer attitude loop (Betaflight's "Level" mode was used sparingly, but we tested angle control in horizon mode for tuning). This loop generates rate commands to drive the vehicle's orientation (roll/pitch angles) to the pilot's stick inputs or to level. In our setup, we mostly fly in rate (acro) mode for forward flight, so a full attitude hold was not heavily used; however, for hover (e.g. in Betaflight's Horizon mode), we adjusted the proportional gains on the attitude controller so that the vehicle would return to upright hover when sticks were centered. Essentially, we treated the attitude controller P-gain as the "stick sensitivity" for leveling. We followed the guideline

of keeping these gains relatively low and letting the fast rate loop do the heavy work. In a tethered test, we started the vehicle slightly perturbed (e.g., 10° off vertical) and released it: the attitude controller brought it back toward vertical. By increasing the attitude P gain, the correction became faster, but too high a value caused a noticeable overshoot (the vehicle would sway past the vertical). Notably, we left the attitude I and D terms at zero (or very low) as is often recommended – the integrator is not needed for a vehicle that has no steady-state angle error in acro mode. The outcome was that the vehicle, when put in a self-level mode, would right itself from ~15° disturbance in under 2 seconds, which is adequate for safety during takeoff.

With rate and attitude loops tuned, the vehicle hovered reliably, responding to pilot inputs in a stable and predictable manner. Further tuning of velocity or position controllers (if needed) follows similar steps, ensuring each layer of control is validated before proceeding.

6.2 Results of Hover Tests

After tuning, the UAV underwent several untethered hover trials to evaluate performance. The vehicle demonstrated stable hovering capabilities. Key hover performance metrics were recorded and are summarized below:

- Power and Current Draw: In a steady hover at ~3 m altitude (no wind), the average throttle required was ~26% of maximum. The power system (running on a 6-cell 1600 mAh LiPo battery) drew about 11.20 A of current at hover, corresponding to approximately 248.6 W of electrical power. The current draw

was well within the ESC and motor limits, and the battery voltage remained stable (no significant sag) at this throttle level. These figures are in line with expectations for a vehicle of this configuration.

Figure 30: Aircraft Maintaining Stable Hover During Indoor Testing

- Hover Stability and Control Precision: With the final PID gains, the UAV could hold an attitude within ±2° in pitch and roll during hover. The yaw heading could be maintained to within ±5° without accumulating drift, thanks to the absence of a yaw integrator wind-up (the differential thrust yaw control proved crisp). There was no sign of oscillatory behavior, indicating the damping was adequate. The controller exhibits a slightly underdamped but well-behaved response (one

overshoot of ~3° and then convergence). This was interpreted as a good trade-off: slightly underdamped means responsiveness, yet the overshoot is minor. Making the attitude loop more sluggish, resulted in slower corrections. The stability margin observed (no oscillation even when we briefly increased P gains by 10% during a test) gives confidence that the UAV can tolerate some changes (like different payload distribution resulting in moderate CG shifts) without immediate retuning.

- Hover Endurance: Using a 6S 1,600 mAh LiPo battery (35.52 Wh), we measured the hover endurance. In a zero-payload configuration, the UAV achieved hover flight times of approximately 8 minutes while draining 80% of its battery (safe landing threshold). The aircraft drew 11.2 A of current at hover along with 248.6 W power. This is the time sustaining a hover; in practice, some periodic lateral movement and small adjustments were made but no significant horizontal flight. The endurance is lower than initial theoretical estimates (~11 min) due to real-world inefficiencies (for example power draw from peripherals like the high-powered video transmitter wasn't accounted for). Still, 8 min is a respectable endurance for a fully 3D-printed VTOL of this scale. We also performed a hover test with a payload of 0.5 kg attached (representing a small sensor package). The added weight required ~40-45% throttle to hover and increased the current draw to ~18.6 A. The hover endurance with this payload dropped to about 5 minutes. We note that pushing the battery further (below 20% remaining) could extend these times by a couple of minutes, but we adhered to safe operating limits.

- Thermal and Electrical Health: During the longest hover trials, we monitored motor and ESC temperatures. The motors warmed to about 65°C (in 28°C ambient) after 4 minutes – warm but within safe limits for brushless outrunners. The ESCs, which have cooling fins but are enclosed in the aircraft, got relatively warm (~50°C). No signs of overheating or voltage regulator issues were observed. The LiPo battery temperature rose modestly (from 20°C to ~30°C). Overall, the electrical system showed healthy performance with no voltage sag or thermal throttling throughout the hover tests.
- Hover Accuracy: While we did not have GPS position hold active for these tests, we anecdotally observed the free hover drift. In calm air, the UAV would drift no more than 1–2 m over a minute of hover, which might be due to slight initial transients and sensor biases. This drift was small enough that it could be manually corrected with tiny stick inputs occasionally. In breezy conditions (2–3 m/s wind), as the UAV's wings buffeted in the wind, it did require a constant uptilt into the wind to hold position, which the pilot provided manually.

In summary, the hover trials validated that the UAV could take off vertically and maintain a stable hover with reliable control. The tuning procedure yielded a flight controller setup that is robust – the vehicle felt "locked in" during hover, with quick responses and no oscillations. The power consumption and flight time are within the expected range for the design. One highlight is that the vehicle's tandem-wing design did not introduce any unexpected instability in hover; sometimes large lifting surfaces can catch wind or induce oscillations, but our controller and perhaps the inherent damping of

the wings (as large flat plates) kept it steady. The success of these hover tests was an essential milestone before attempting any transition to forward flight.

6.3 Transition Test Procedures and Safety Measures

With stable hover achieved, the next step was testing the transition to forward flight. These tests were conducted in a wide-open field on calm days, with a focus on manual control since the flight controller did not have an automatic transition mode.

Figure 31 – Aircraft Transition from Fixed Wing to Vertical Flight

- Pre-Transition Hover: The UAV would take off vertically and hover at about 10–15 m altitude. This altitude was chosen to provide enough buffer for recovery in case the transition did not go as planned. The vehicle was yawed to point into any prevailing wind (to minimize weathercocking issues).

- Initial Pitch-Over Maneuver: The pilot then gently pushed the pitch stick forward to start tilting the nose down from the vertical attitude. Our plan was to execute a slow, controlled transition (as opposed to a rapid flip). As the nose pitched ~30° forward from vertical, the flight controller was still primarily using thrust vectoring to control attitude. At this stage, both motors still provided significant lift and some horizontal components. The pilot increased throttle slightly (~70%) during the pitch-forward to ensure the UAV had enough thrust to not lose altitude as the lift vector reoriented. Essentially, we traded some vertical thrust for horizontal acceleration.

- Mid-Transition (45–60° Tilt): In this intermediate angle, the UAV is neither fully a quadcopter nor an airplane. The forward wing started to generate some lift as airspeed built up, and the weight began to be supported by aerodynamic lift in addition to thrust. We monitored this as the aircraft struggled to gain airspeed with the portion of the lift vector pointing back until additional throttle was added. Meanwhile, we had to manage the yaw-roll coupling: as the craft tilted, any yaw input from the pilot (which in hover rotated the nose) would now cause the aircraft to bank. The pilot, flying FPV, compensated by using a mix of yaw and

roll inputs to keep the wings level through the transition. Similar dynamics are observed when transitioning back from forward to hover flight.

- Completion to Level Flight: As the UAV approached ~80–90° tilt (almost level), the pilot leveled off the pitch input and eased the throttle to cruise setting. At this point, we effectively had a fixed-wing aircraft flying forward. The transition was complete when the aircraft's weight was fully supported by aerodynamic lift and the motors were primarily providing forward thrust. In practice, our first transition was done at around 20 m altitude with a forward speed of roughly 15 m/s (from GPS data). Once in horizontal flight, the aircraft was flown straight ahead to gain speed and stability.

6.4 Forward Flight Performance

Once the UAV was in forward flight (airplane mode), we assessed its performance as a fixed-wing aircraft. Immediately noticeable was the vehicle's natural stability in cruise compared to the initial "I" frame configuration. The tandem-wing configuration and proper CG placement resulted in a positive static stability margin. In level flight at about 20 m/s, the aircraft maintained straight and level flight with only minor oscillations. This meant that unlike in hover, where constant active corrections are required, in cruise the flight controller (still in acro mode) could be largely hands-off. The pilot essentially had to only make occasional inputs to counter wind or to initiate gentle turns.

Control authority in forward flight was found to be adequate but took some getting used to, especially since aircraft controls very differently than a conventional

aircraft with control surfaces. Near stall conditions, aircraft was difficult to control and necessitated either rapid increase in throttle to gain forward airspeed or to switch to hover flight. Therefore, most transitions from forward flight to hover tend to gain altitude as aircraft pitched gradually pitched up while still staying above stall before the pilot had time to switch back to hover.

We conducted multiple passes over the field at different throttle settings to characterize cruise performance. At ~30% throttle (the same as hover throttle), the airspeed settled around 15 m/s and the aircraft was in a slight nose-up attitude. Pushing to ~45% throttle, we achieved a faster cruise ~20 m/s, at which point the aircraft flew more level and the wings were generating just enough lift to support weight without large nose-up attitude. The current draw at this cruise was about 9.6 A (down from 11 A needed for static hover), showing that wing-borne flight is more efficient for covering distance. We estimate the cruise power around 206 W (or around 50 W per motor, as initially estimated in Section 4.2), considerably lower than hover power (~248.6 W), which matches the expectation that once on the wing, the required power drops.

From these numbers, we can estimate the endurance and range in forward flight. With a 35.52 Wh battery and ~206 W draw, pure cruise flight time is roughly 10.3 minutes equating to approximately 11.7 km range. Realistically, accounting for 30% of flight in hover and transition segments while rest in cruise, about 7 minutes of useful forward flight is achievable. This aligns well with our pre-flight MATLAB theoretical analysis which predicted ~8 min endurance at optimal speed. In the actual flight, we did

not attempt anywhere near that distance (the flights were within line of sight, on the order of 200–300 m downrange).

The same tests with a 0.5 Kg payload needed 55% throttle to reach cruise which was at a higher-than-expected velocity of 28 m/s, while drawing 18.4 A current at 396 W. Giving us a cruise only range of 8.5 Km. Accounting for time spent in hover and transition, the effective range with payload is closer to 4.5-5 Km which is about 1.5 km less than theoretical predictions, for this battery size. Differences can be attributed to unmodeled factors like power draw from peripherals, efficiency drop at certain throttle levels and modeling limitations with VSPAero's panel method.

CHAPTER 7

AIRWORTHINESS

7.1 Overview of FAA Categories and Thresholds

Under the FAA's updated regulations for small, unmanned aircraft (Part 107, Operations Over People), drones are classified into Categories 1 through 4 based on their weight, potential injury severity, and safety mitigations (such as rotating-part protections or parachutes). Category 2 allows operations over people if the drone does not exceed a specific kinetic energy transfer threshold upon impact (11 ft-lb ~ 15 J of energy transfer).

FAA rules prescribe that the UAV must not cause injury to a human being that is equivalent to or greater than the severity of injury caused by a transfer of 11 foot-pounds (ft-lbs) of kinetic energy upon impact from a rigid object (Machnik, 2021). Meeting or staying below these impact energy levels typically satisfies the intent of Category 2: that the risk of serious injury is significantly reduced. To demonstrate compliance, manufacturers often provide validated impact analyses—either through physical drop tests or high-fidelity simulations. Here, we employed conservative Abaqus simulations to examine multiple free-fall scenarios from an altitude of 400 feet, with and without drag, as well as a lower-velocity impact case facilitated by a parachute to ensure the worst-case scenarios were accounted for.

7.2 Simulation Approach using Abaqus

Three impact velocities were evaluated to gauge the drone's worst-case and mitigated collision energies. In all scenarios, the drone mass was set to the final flight configuration (1.5 kg), and the geometry was modeled to reflect the fuselage, wings, and key structural elements. For modelling the head, average material properties of a skull (most rigid part of the head) were used to better visualize the impact area and size. Damage to the aircraft was not a concern so it was modeled as an analytical rigid body, with the same mass properties as the real drone.

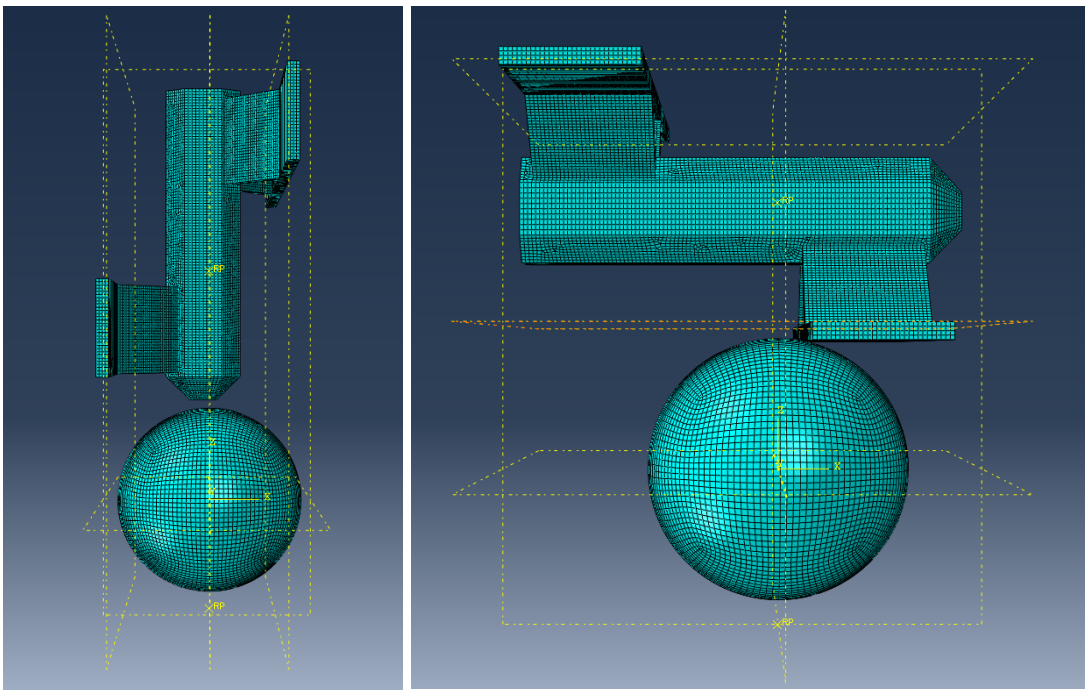

Figure 32: Mesh Model of Nose Down Impact (left) and Wing Impact (right)

Case 1: Free Fall from 400 ft (No Drag)

A pure ballistic scenario, ignoring aerodynamic drag. Calculations show the drone reaching roughly 50 m/s (≈ 180 km/h) before impact, equating to a potential collision energy near the upper bound for a drone of this mass.

Case 2: Free Fall from 400 ft (With Drag)

If the object is dropped from a great enough height, it eventually reaches a constant speed called the terminal velocity. At terminal velocity, the drag force exactly balances the gravitational force.

$$Mg = \frac{1}{2}\rho V^2 A C_d \quad [9]$$

Solving for V gives:

$$V = \sqrt{\frac{2Mg}{\rho A C_d}} \approx 40 \text{ m/s} \quad [30]$$

Here, M is mass of our UAV, $g = 9.81$ m/s^2 is the acceleration due to gravity, ρ = air density, $A = 124$ cm^2 frontal area of the aircraft and C_d is drag coefficient as calculated in [6]. As discussed in next section, this more realistic scenario already reduces total collision energy by a significant margin compared to the no-drag case.

Case 3: Impact with Deployed Parachute

An off-the-shelf parachute is assumed to limit descent velocity to 4.6 m/s. This condition greatly lowers the impact energy and is typically consistent with Category 2 energy requirements given the parachute can reliably deploy in the event of system failures.

To account for worst-case orientation, each velocity was tested in two drone attitudes, Nose Down (minimal Surface area), and wing edge impact (sharper cross section). These orientations were chosen to encompass both a smaller contact footprint and a thin edge collision—two extremes likely to yield high localized stresses on the airframe and potentially higher injury risk.

7.3 Simulation Results and Implications

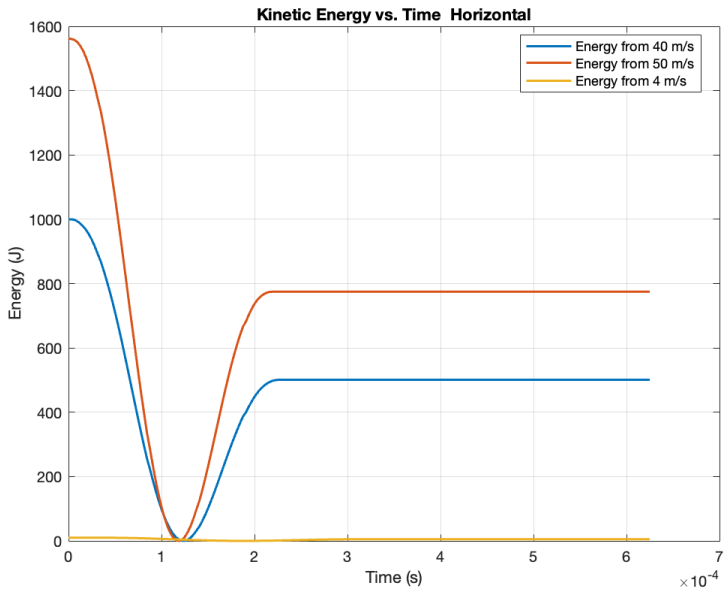

Figure 32: Kinetic energy vs time curve for the aircraft for belly up attitude

No-Drag Condition (Case 1):

As one can expect free-fall at 50 m/s resulted in higher energy transfer than the 15 J threshold set by FAA. In total, 800 J of Kinetic energy transferred to the skull. Moreover, in figure 33 we can see the high concentration of stresses at point of impact.

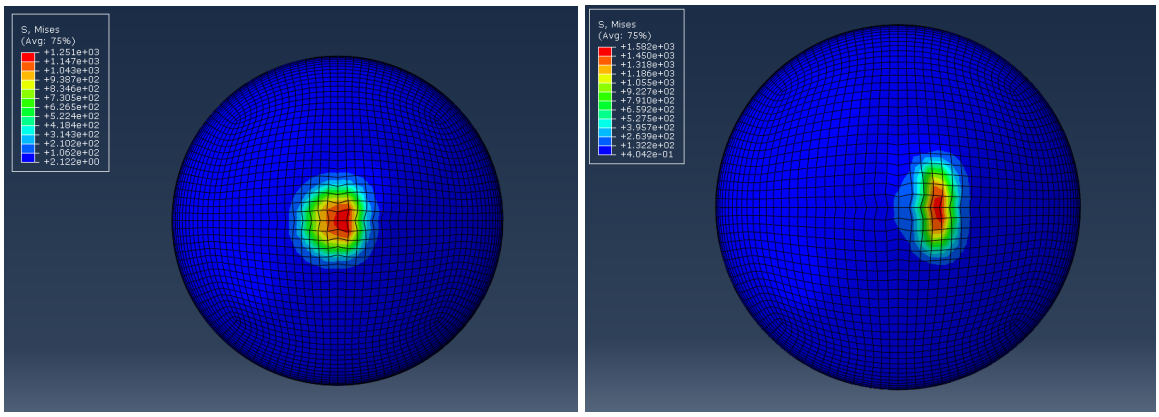

Figure 33: Von Mises Stress Contours for No Drag Free Fall

Free Fall with Drag Condition (Case 2):

At ≈ 40 m/s, maximum stress levels remained significant but were notably lower than the no-drag case. The energy transfer still exceeded the kinetic energy ceiling for Category 2 compliance without a parachute.

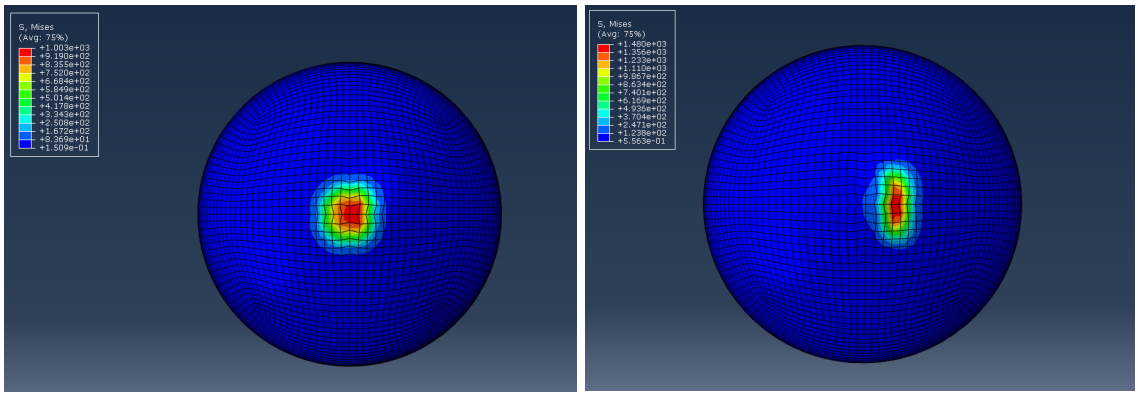

Figure 34: Von Mises Stress Contours for Free Fall with Drag

Parachute-Enabled Impact Condition (Case 3):

4.6 m/s descent velocity cuts the kinetic energy by an order of magnitude compared to the no-drag scenario, yielding more benign impact outcomes in both nose-down and wing-edge attitudes. Calculated impact energies (10 J) and stress levels fell under the

referenced Category 2 threshold (under ~11 ft-lb or ~16 J), indicating a considerably lower risk of severe injury.

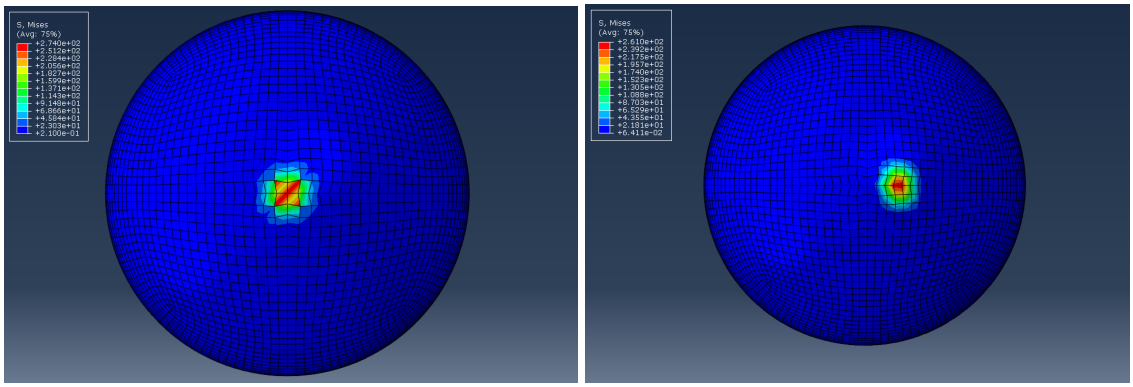

Figure 33: Von Mises Stress Contours for Impact with Parachute Deployed

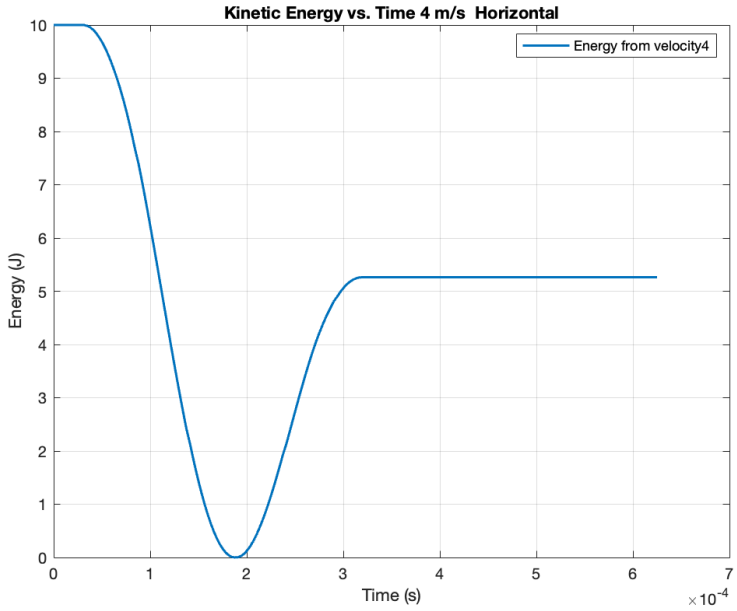

Figure 34: Kinetic energy vs Time for case with parachute (belly up attitude)

CHAPTER 8

CONCLUSION AND FUTURE WORK

8.1 Conclusion

This thesis set out to develop a tandem-wing tailsitter UAV capable of sustaining both efficient forward flight and precise vertical takeoff/landing behavior without resorting to complex tilt-rotor mechanisms. By consolidating lessons from earlier eVTOL research, drawing on tandem-wing theory, and implementing a gull/inverted-gull configuration, the project sought a balance between aerodynamic efficiency, controllability, and structural simplicity. The final prototype addressed several key obstacles identified in the early stages of design—most notably, achieving adequate torsional rigidity in the fuselage and mitigating pitch-instability tendencies inherent to tandem-wing layouts. Ultimately, careful allocation of wing incidence, dihedral/anhedral angles, and differential motor thrust allowed the UAV to transition smoothly from vertical hover to forward cruise flight, confirming many of the performance predictions from VSPAero analyses.

A major determinant of success was the structural strategy of combining 3D-printed fuselage sections with carbon-fiber spars. This integration not only provided a robust skeleton capable of handling aerodynamic loads during forward flight but also resisted the twisting moments that arise from differential thrust in hover and transition. Ground tests showed that torsional stresses were significantly reduced once the fuselage and wing-root interfaces were redesigned to include internal ribs and support rods, underscoring the importance of iterative testing in UAV development. Equally critical

was the selection of motor-propeller combinations that balance hover thrust requirements with forward-flight efficiency. Although the smaller tri-blade props proved slightly less efficient during hover than large-diameter, low-pitch rotors, they delivered better performance at cruise speeds, confirming the versatility needed for a multi-regime design.

Flight tests in both indoor and outdoor environments validated the fundamental viability of this UAV concept. During hover trials, the vehicle's responsiveness to pilot inputs demonstrated reliable roll, pitch, and yaw control—particularly once the PID loops for the rate and attitude controllers were optimized. Transition tests further revealed that the design's forward CG placement and front-wing incidence offset facilitated stable nose-down rotation into horizontal flight. In forward flight, the tandem-wing arrangement distributed lift more evenly than a single-main-wing design, and the elevated rear gull section minimized wake interference. Even though real-world performance slightly lagged behind idealized estimates—particularly in achievable range and exact stall speeds—such deviations are common in prototyping phases, where aerodynamic assumptions meet practical constraints like battery load, additional electronics, and surface irregularities. Overall, the prototype effectively showcased a mechanically simpler alternative to tilt-rotor UAVs, one that can deliver integrated VTOL and level-flight capabilities via a unified four-motor setup.

Despite the encouraging results, the investigation also highlighted areas that can benefit from deeper exploration. The UAV's control scheme still relies heavily on motor thrust in forward flight, which can lead to higher power consumption under certain conditions. The aerodynamic interplay between front and rear wings during rapid

transitions or gusty conditions remains a point of interest for more rigorous simulation and wind tunnel validation. Nevertheless, the fundamental outcome of this work is a tangible, sub-scale aircraft that demonstrates the viability of a tandem gull-wing tailsitter eVTOL. By providing a promising blend of design simplicity, structural stability, and aerodynamic efficiency, this prototype lays the groundwork for more advanced UAV designs that could be scaled, optimized, and potentially adapted to specialized missions involving rapid deployment of payloads or precision landings in confined spaces.

Ultimately, this research highlights the potential of VTOL layouts that step away from traditional tiltrotor and hybrid propulsion complexity. The tandem-wing tailsitter tested here underscores that, with deliberate aerodynamic analysis and iterative structural refinement, UAVs can operate proficiently in both hover and fixed-wing modes while retaining a streamlined control architecture and robust frame. Future design work can build on these insights to further push the boundaries of efficiency, payload capacity, and operational flexibility in modern UAV applications. By bridging these important technical gaps, this thesis aims to advance the next generation of tailsitter platforms and, more generally, eVTOL vehicles aspiring to fill niche but significant roles in aerial logistics, surveillance, and emergency response.

8.2 Future Work

Although the prototype validated core aspects of the tandem wing tailsitter design, several potential areas could further expand the aircraft's performance and reliability. More sophisticated aerodynamic studies, possibly including wind tunnel testing and refined CFD analyses, would help capture aerodynamic interactions between front and

rear wings under dynamic transition conditions. Incorporating active control surfaces on the wings for forward flight could reduce power consumption by allowing lower motor RPMs and finer control of roll, pitch, and yaw. Future efforts might also explore high-lift propellers or variable-pitch propeller systems that optimize efficiency for both hover and cruise.

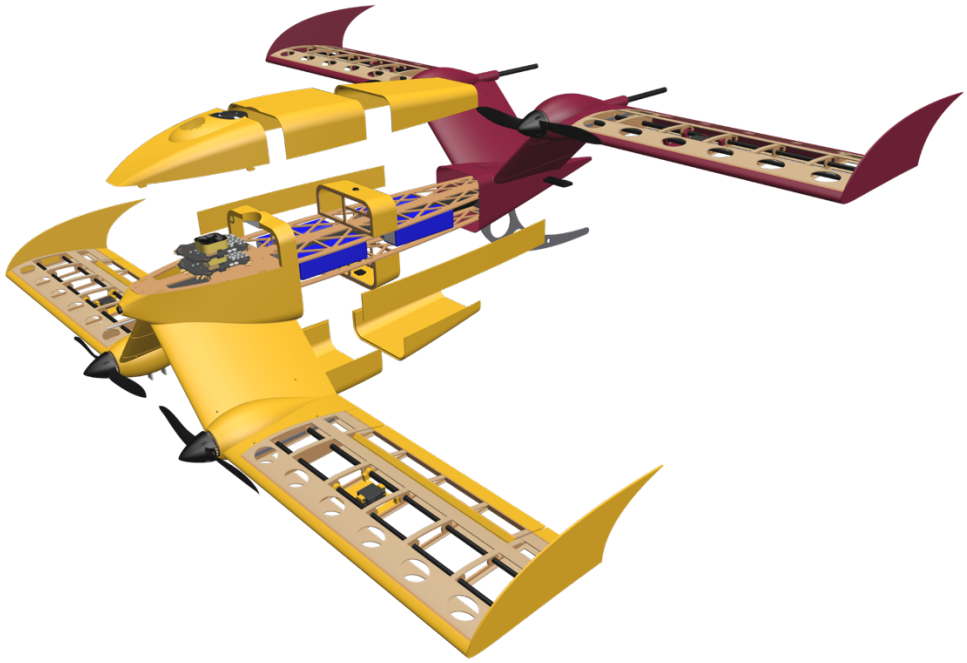

Figure 35 – Exploded View of Scaled Up Version of the Aircraft

Additional improvements in structural design, such as the selective use of lightweight composite materials or advanced infill patterns, could yield a more rigid airframe with lower mass. This would enhance flight performance and potentially allow greater payload capacity. A more robust flight control system that automates the hover-to-forward-flight transition would also help minimize pilot workload and mitigate errors. For applications requiring safe operations over populated areas, integration of a low-cost parachute

recovery system should be investigated. As a longer-term extension, scaling the platform to carry heavier payloads or operate for extended durations would require additional testing of power systems, propulsion layouts, and advanced autonomy algorithms. Through these refinements, the fundamental tandem-wing tailsitter concept can be extended to a broader range of UAV missions, maintaining simplicity in flight operation alongside meaningful gains in efficiency and reliability.

REFERENCES

Bacchini, A., & Cestino, E. (2019). Electric VTOL Configurations Comparison. *Aerospace*, *6*(3), 26. https://doi.org/10.3390/aerospace6030026

Figat, M. (2022). A strategy of the longitudinal control for the tandem wing configuration design. *Aircraft Engineering and Aerospace Technology*, *95*(1), 155–169. https://doi.org/10.1108/aeat-12-2021-0372

Andrews, S., & Perez, R. (2017). Analytic study of the conditions required for longitudinal stability of dual-wing aircraft. *Proceedings of the Institution of Mechanical Engineers Part G Journal of Aerospace Engineering*, *232*(5), 958–972. https://doi.org/10.1177/0954410017704215

Zhang, Q., Xue, R., & Li, H. (2023). Aerodynamic Exploration for Tandem Wings with Smooth or Corrugated Surfaces at Low Reynolds Number. *Aerospace*, *10*(5), 427. https://doi.org/10.3390/aerospace10050427

Kostić, I., Simonović, A., Kostić, O., Ivković, D., & Tanović, D. (2024). Lateral-Directional Aerodynamic Optimization of a Tandem Wing UAV Using CFD Analyses. *Aerospace*, *11*(3), 223. https://doi.org/10.3390/aerospace11030223

Barbosa, A. a. F., Catalano, F. M., & University of Sao Paulo (EESC-USP). (2021). INFLUENCE OF GULL WING ON LONGITUDINAL AND LATERAL-DIRECTIONAL COEFFICIENTS OF AN AIRPLANE. In *University of Sao Paulo (EESC-USP)* (Vol. 1, pp. 1–3) [Journal-article]. https://www.icas.org/icas_archive/ICAS2018/data/papers/ICAS2018_0670_paper.pdf

Scholz, D. (2021). Empennage sizing with the tail volume complemented with a method for dorsal fin layout. INCAS BULLETIN, 13(3), 149–164.

Šančić, T., Brčić, M., Kotarski, D., & Łukaszewicz, A. (2023). Experimental Characterization of Composite-Printed Materials for the Production of Multirotor UAV Airframe Parts. *Materials*, *16*(14), 5060. https://doi.org/10.3390/ma16145060

Ardupilot Tailsitter Planes — Plane documentation. (n.d.). https://ardupilot.org/plane/docs/guide-tailsitter.html

Machnik, M. (2021). Operation of Small Unmanned Aircraft Systems Over People. *Federal Aviation Administration*. https://www.faa.gov/sites/faa.gov/files/2021-08/OOP_Final%20Rule.pdf

APPENDIX A

AIRFOIL TRADE STUDIES

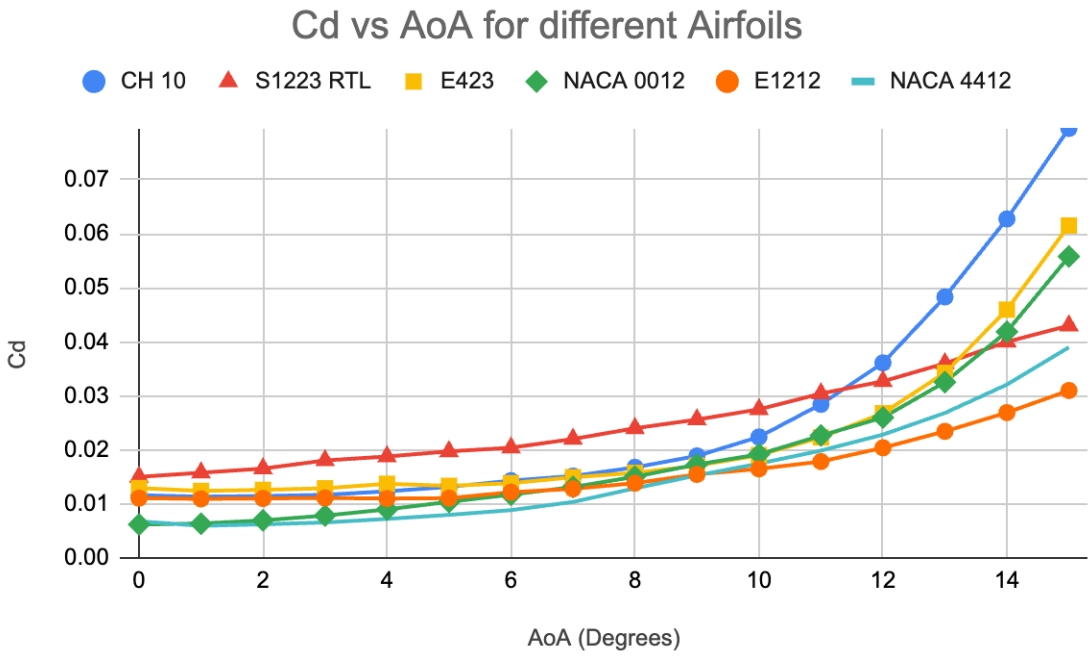
Cd vs AoA for different Airfoils
CH 10
S1223 RTL
E423
NACA 0012
E1212
NACA 4412
Cd
0.07
0.06
0.05
0.04
0.03
0.02
0.01
0.00
0
2
4
6
8
10
12
14
AoA (Degrees)

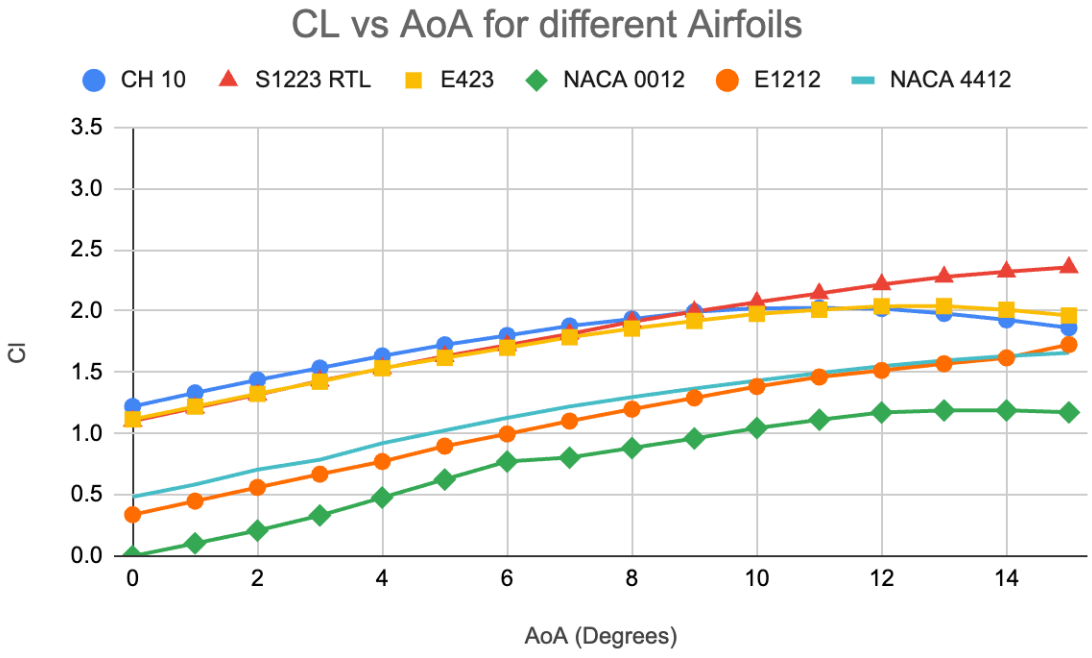
CL vs AoA for different Airfoils
CH 10
S1223 RTL
E423
NACA 0012
E1212
NACA 4412
Cl
3.5
3.0
2.5
2.0
1.5
1.0
0.5
0.0
0
2
4
6
8
10
12
14
AoA (Degrees)

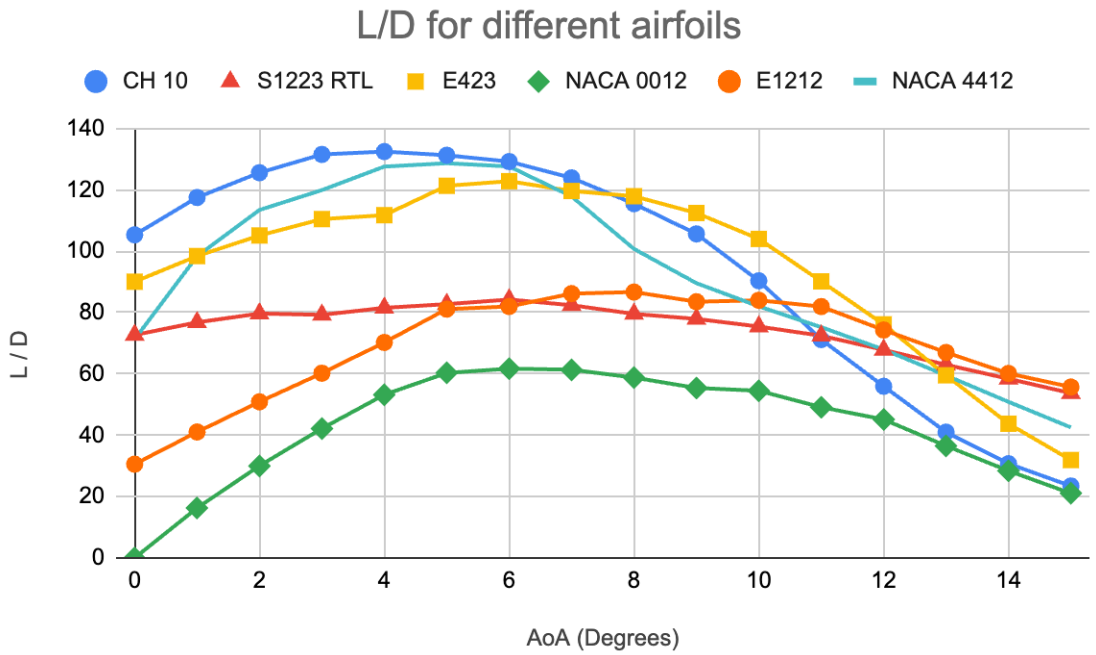

NACA 4412 - NACA 4412 airfoil

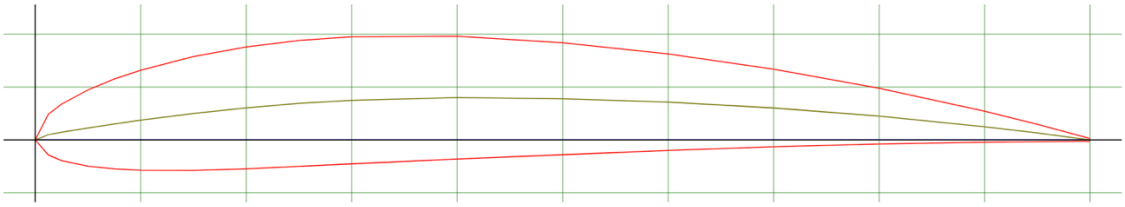

CH10 (smoothed) - Chuch Hollinger CH 10-48-13 high lift low Reynolds number airfoil

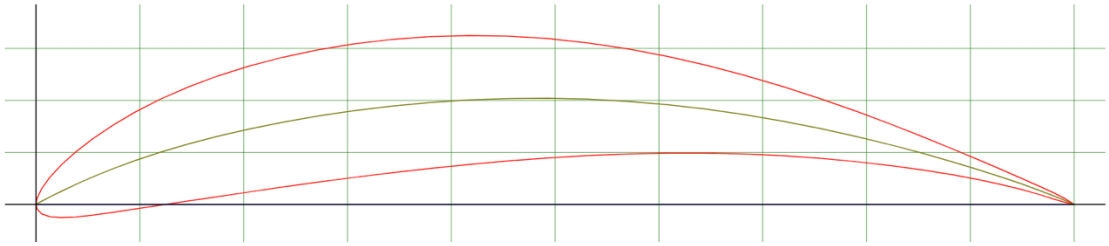

S1223 - Selig S1223 high lift low Reynolds number airfoil

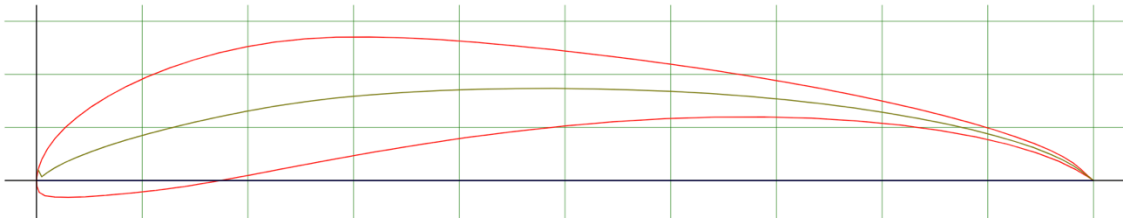

E423 - Eppler E423 high lift airfoil

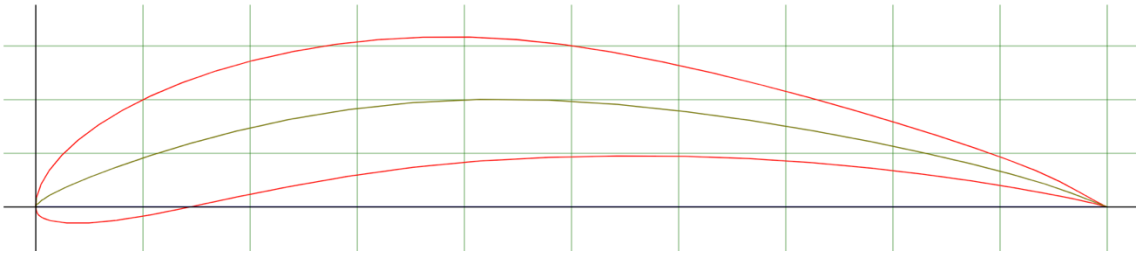

EPPLER E1212 AIRFOIL - Eppler E1212 general aviation airfoil

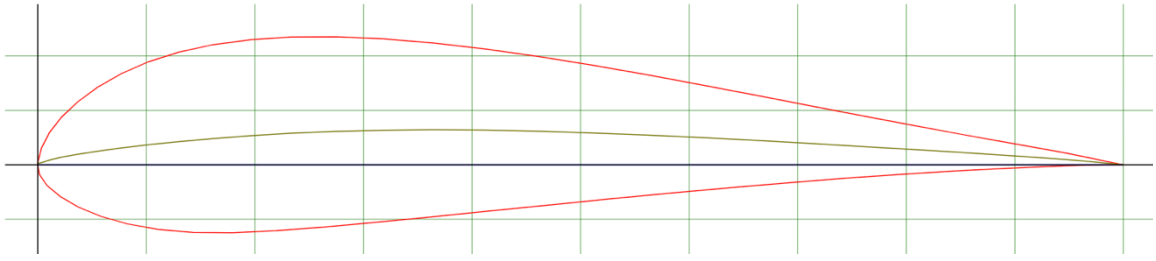

NACA 0012 AIRFOILS - NACA 0012 airfoil

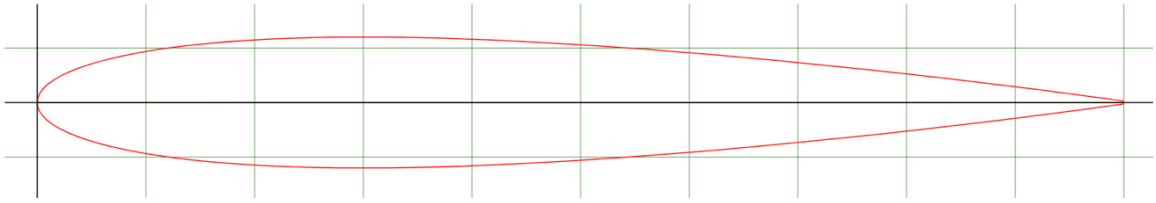

APPENDIX B

MATLAB PERFORMANCE ESTIMATION CODE

```
% Fixed parameters:
mass_struct    = 1.5 - 0.225;             % structural mass (excluding ~0.225 kg for 1400mAh battery)
battery_caps   = 800:200:10000;           % test 800mAh to 3000mAh
hover_fraction = 0.3;                    % 30% hover time

% Pre-allocate arrays to store results
range_vals  = zeros(size(battery_caps));
speed_vals  = zeros(size(battery_caps));
weight_vals = zeros(size(battery_caps));  % <-- new array to store total (takeoff) weight

% Calculate and store range, speed, and total weight for each capacity
for i = 1:length(battery_caps)
    cap = battery_caps(i);

    % Compute range and speed using your function
    [rng_m, speed_m_s] = compute_range_and_speed(cap, mass_struct, hover_fraction);

    % Also replicate the battery-mass calculation to track total weight
    batt_mass    = 0.225 * (cap / 1400) + (0.225 * (cap / 1400))/3;   % from inside function
    total_mass   = mass_struct + batt_mass;
    weight_vals(i) = total_mass;  % (kg)

    range_vals(i) = rng_m;        % in meters
    speed_vals(i) = speed_m_s;    % in m/s

    fprintf('%d mAh -> Range: %.1f km, Cruise Speed: %.1f m/s, Total Weight: %.2f kg\n',...
            cap, rng_m/1000, speed_m_s, total_mass);
end

% ---- Plot Battery Capacity vs. Range
figure;
plot(battery_caps, range_vals/1000, 'o-', 'LineWidth',1.2);
xlabel('Battery Capacity (mAh)');
ylabel('Range (km)');
title('Battery Capacity vs. Range');
grid on;

% ---- Plot Battery Capacity vs. Speed
figure;
plot(battery_caps, speed_vals, 'o-', 'LineWidth',1.2);
xlabel('Battery Capacity (mAh)');
ylabel('Cruise Speed (m/s)');
title('Battery Capacity vs. Cruise Speed');
grid on;

% ---- Plot Battery Capacity vs. Total Weight
figure;
plot(battery_caps, weight_vals, 'o-', 'LineWidth',1.2);
hold on;
% Red dashed line at 3 kg:
yline(3, 'r--', 'LineWidth',1.2);
hold off;
xlabel('Battery Capacity (mAh)');
ylabel('Total Weight (kg)');
title('Battery Capacity vs. Total Weight');
grid on;
```

```
%% ================================
%  FUNCTION: compute_range_and_speed
%  ================================
function [rng, V] = compute_range_and_speed(cap_mAh, mass_struct, hover_frac)
    %{
       Returns:
           rng (m) - total range in meters
           V (m/s) - cruise speed in m/s
    %}

    % Assumed linear scaling of battery mass (same logic as main script):
    batt_mass  = 0.225 * (cap_mAh / 1400) + (0.225 * (cap_mAh / 1400))/4;
    total_mass = mass_struct + batt_mass;   % total takeoff mass (kg)
    W          = total_mass * 9.81;         % weight (N)

    rho = 1.18;        % air density (kg/m^3)
    S   = 0.116;       % reference area (m^2)

    % lift coefficient:
    CL = 0.5;
    % Solve for cruise speed based on lift = weight:
    V = sqrt( 2*W / (rho * CL * S) );

    % Estimate parasite + induced drag:
    % (CD_0 = 0.05, AR=6.88, e=0.8)
    CD = 0.05 + CL^2 / (2*pi * 6.88 * 0.8);

    % Cruise drag force (N):
    D = 0.5 * rho * V^2 * S * CD;

    % Cruise power (W), assuming ~0.6 prop efficiency:
    P_cruise = D * V / 0.7;

    % Hover power (momentum theory):
    A_total  = 4 * pi * (0.127 / 2)^2;  % total rotor area
    vi       = sqrt(W / (2 * rho * A_total));
    P_hover  = W * vi / 0.6;

    % Available battery energy (J):
    %   (cap_mAh / 1000) -> Ah
    %   nominal Voltage = 22.2 V
    %   3600 s per hour
    %   0.8 discharge fraction
    E = (cap_mAh / 1000) * 22.2 * 3600 * 0.8;

    % Average power draw (W):
    P_avg = hover_frac * P_hover + (1 - hover_frac) * P_cruise;

    % Total flight time (s):
    t_total = E / P_avg;

    % Time spent in cruise:
    t_cruise = (1 - hover_frac) * t_total;

    % Distance covered during cruise (m):
    rng = V * t_cruise;
end
```